

Long-Term Single-Column Model Intercomparison of Diurnal Cycle of Precipitation Over Midlatitude and Tropical Land

Shuaiqi Tang¹, Shaocheng Xie^{2*}, Zhun Guo³, Song-You Hong⁴, Boualem Khouider⁵, Daniel Klocke^{6#}, Martin Köhler⁷, Myung-Seo Koo⁸, Phani Murali Krishna⁹, Vincent E. Larson^{10,1}, Sungsu Park¹¹, Paul A. Vaillancourt¹², Yi-Chi Wang¹³, Jing Yang¹², Chimene Laure Daleu¹⁴, Cameron R. Homeyer¹⁵, Todd R. Jones¹⁴, Neelam Malap⁹, Roel Neggers¹⁶, Thara Prabhakaran⁹, Enver Ramirez¹⁷, Courtney Schumacher¹⁸, Cheng Tao², Peter Bechtold¹⁹, Hsi-Yen Ma², J. David Neelin²⁰, and Xubin Zeng²¹

1. Pacific Northwest National Laboratory, Richland, WA, USA
2. Lawrence Livermore National Laboratory, Livermore, CA, USA
3. Climate Change Research Center, Institute of Atmospheric Physics, Chinese Academy of Sciences, Beijing, China.
4. NOAA/Earth System Research Laboratory and CIRES/University of Colorado, Boulder, CO, USA
5. Department of Mathematics and Statistics, University of Victoria, Victoria, BC, Canada
6. Hans Ertel Centre for Weather Research, Deutscher Wetterdienst, Offenbach, Germany
- 7.
8. Korea Institute of Atmospheric Prediction Systems, Seoul, South Korea
9. Indian Institute of Tropical Meteorology, Pune, India
10. Department of Mathematical Sciences, University of Wisconsin-Milwaukee, Milwaukee, WI, USA
11. School of Earth and Environmental Sciences, Seoul National University, Seoul, South Korea
12. Meteorology Research Division, Environment and Climate Change Canada, Dorval, Québec, Canada
13. Research Center for Environmental Changes, Academia Sinica, Taipei, Taiwan
14. Department of Meteorology, University of Reading, Reading, UK.
15. School of Meteorology, University of Oklahoma, Norman, OK, USA
16. Institute of Geophysics and Meteorology, University of Cologne, Cologne, Germany
17. Numerical Modeling and Development Division, Center for Weather Forecasting and Climate Studies, National Institute for Space Research, São Paulo, Brazil
18. Department of Atmospheric Sciences, Texas A&M University, College Station, TX, USA

37 19. European Centre for Medium-Range Weather Forecasts, Reading, UK

38 20. Dept. of Atmospheric and Oceanic Sciences, University of California in Los Angeles,
39 Los Angeles, CA, USA

40 21. Department of Hydrology and Atmospheric Sciences, University of Arizona, Tucson,
41 AZ, USA

42
43 # now at Max-Planck-Institut für Meteorologie, Hamburg, Germany

44
45
46
47
48
49
50
51
52
53
54
55
56 Contact: Shaocheng Xie (xie2@llnl.gov)

59 General Circulation Models (GCMs) have for decades exhibited difficulties in modeling the
60 diurnal cycle of precipitation (DCP). This issue can be related to inappropriate representation of
61 the processes controlling sub-diurnal phenomena like convection. In this study, eleven single-
62 column versions of GCMs are used to investigate the interactions between convection and
63 environmental conditions, processes that control nocturnal convections, and the transition from
64 shallow to deep convection on diurnal time scale. Long-term simulations are performed over two
65 continental land sites: the Southern Great Plains (SGP) in the U.S. for twelve summer months
66 from 2004 to 2015 and the Manacapuru site at the central Amazon (MAO) in Brazil for two full
67 years from 2014 to 2015. The analysis is done on two regimes: afternoon convective regime and
68 nocturnal precipitation regime. Most models produce afternoon precipitation too early, likely due
69 to the missing transition of shallow-to-deep convection in these models. At SGP, the unified
70 convection schemes better simulate the onset time of precipitation. At MAO, models produce
71 heating peak in a much lower level comparing with observation, indicating too shallow
72 convection in the models. For nocturnal precipitation, models that produce most of nocturnal
73 precipitation all allow convection to be triggered above the boundary layer. This indicates the
74 importance of model capability to detect elevated convection for simulating nocturnal
75 precipitation. Sensitivity studies indicate that (1) nudging environmental variables towards
76 observations has a minor impact on DCP; (2) unified treatment of shallow and deep convection
77 and the capability to capture mid-level convection can help models better capture DCP; and (3)
78 the interactions of the atmosphere with other components in the climate system (e.g., land) are
79 also important for DCP simulations in coupled models. These results provide long-term
80 statistical insights on which physical processes are essential in climate models to simulate DCP.

1. Introduction

The diurnal cycle of precipitation (DCP) is one of the most important signals affecting climate variability and weather forecasting. Although it is dominated by diurnal variation of solar insolation that greatly affects the surface energy budget and regulates surface temperature (Dai et al. 1999), mesoscale propagating systems and large scale envelopes are also responsible for regulating DCP (e.g., Rutledge and Hobbs 1984; Wei et al. 2020). As a benchmark for evaluating climate models (Covey et al. 2016), DCP provides an excellent measure of how well climate models simulate not only the total amount of precipitation but also its frequency, intensity, timing and duration (Trenberth et al. 2003).

General Circulation Models (GCMs) have for decades exhibited difficulties in modeling the diurnal precipitation. Dai (2006) examined 18 GCMs and found that many models showed peak precipitation around noontime over land and around 02 local standard time (LST) over ocean, both a few hours earlier than observations. Covey et al. (2016) examined 24 models from phase 5 of the Coupled Model Intercomparison Project (CMIP5, Taylor et al. 2012), and found similar biases; i.e. GCMs produce warm season rainfall too early in the day. Recently, Fiedler et al. (2020) and Tang et al. (2021) examined the latest GCMs from CMIP6 (Eyring et al. 2016) compared with earlier CMIP versions. They found that although CMIP6 models have made improvements on DCP, they still suffer from the same problems: producing rainfall too early in the day over land and missing nocturnal rainfall peak associated with elevated convection and propagating mesoscale convective systems (MCSs).

These issues in simulating DCP in climate models can be related to inappropriate representation of the processes that control sub-diurnal phenomena like convection, and phenomena with timescales of several hours, like MCSs. Many studies attribute the model biases in DCP to the deficiencies in convective parameterizations (e.g., Koo and Hong 2010). Great efforts have been made to improve DCP in GCMs by improving the convective trigger (e.g., Xie and Zhang 2000; Bechtold et al. 2004; Rio et al. 2009; Wang and Hsu 2019; Xie et al. 2019), closure (e.g., Zhang 2003; Rio et al. 2009; Bechtold et al. 2014), entrainment and detrainment rates (e.g., Wang et al. 2007; Bechtold et al. 2008; Stratton and Stirling 2012), or the detection of mid-level convection that is related to the nocturnal precipitation peak over regions such as the central U.S. (e.g., Lee et al. 2008; Wang et al. 2015; Xie et al. 2019; McTaggart-Cowan et al. 2020). Other parameterizations (e.g., Park 2014a, 2014b; Neggers 2015a; Guo et al. 2021) that unify the deep convective scheme with other parameterizations also provide a path toward improving DCP simulation. One of the challenges is the difficulty to find parametric formulations that are valid for both shallow and deep convection (Del Genio 2012), which have quite different underlying physical processes. Another challenge is understanding how the different physical processes evolve from one to the other, and how to represent them in models. This drives intense research into convective transitions, including various recent meteorological field campaigns dedicated to this problem (e.g., CACTI, Varble et al. 2021).

A single-column model (SCM) is a useful tool to test physical processes within a column of a GCM (Randall et al. 1996; Zhang et al. 2016; Lin and Xie 2021). In the past twenty years, several SCM intercomparison studies have been organized, focusing on summertime continental convection (Ghan et al. 2000; Xie et al. 2002; Guichard et al. 2004), springtime midlatitude frontal clouds (Xie et al. 2005; Xu et al. 2005), shallow-cumulus clouds over mid-latitude land (Lenderink et al. 2004), marine stratocumulus-topped boundary layers (Bretherton et al. 1999; Zhu et al. 2005; Wyant et al. 2007; Neggers et al. 2017), mixed-phase clouds in the polar region (Klein et al. 2009; Morrison et al. 2009; Pithan et al. 2016) and deep convection over the tropical ocean (Bechtold et al. 2000; Davies et al. 2013; Petch et al. 2014). These intercomparison studies serve as testbeds for developing new parameterizations. For DCP, SCMs produce a similar diurnal structure of precipitation as the full 3-D GCM and are thus suitable to be used as a simplified model of GCMs to explore the physical processes related to DCP (Betts and Jakob 2002).

The above-mentioned SCM intercomparison studies mainly focused on case studies. However, short-term simulations of a few days or a few weeks may not long enough to build robust statistics for phenomena such as DCP [since simulated diurnal peak may be determined by a few strong precipitation events and is largely controlled by the specified large-scale forcing](#). For example, a 42-day simulation during The Midlatitude Continental Convective Clouds Experiment (MC3E, Jensen et al. 2016) shows that most models in this study perform well on nighttime precipitation (Figure 1), which is inconsistent with what has been shown in their climate simulations (e.g., Tang et al. 2021) and the finding from multi-year SCM simulations shown later in this work (Section 3). In recent years efforts have been made to pursue longer-term SCM simulations at permanent meteorological sites (Neggers et al. 2012). In certain conditions this allows direct attribution of persistent biases in GCMs to parameterized subgrid-scale processes (Neggers and Siebesma 2013; Neggers 2015b). In the recent Global Atmospheric System Studies (GASS) Diurnal Cycle of Precipitation intercomparison project (<https://portal.nersc.gov/project/capt/diurnal/>), we are attempting to build robust statistics of the diurnal cycle of precipitation using long-term simulations from various weather and climate models. Two research sites from the Atmospheric Radiation Measurement (ARM) program, Southern Great Plains (SGP) site in the central U.S. and the Manacapuru (MAO) site for the Green Ocean (GoAmazon2014/5, Martin et al. 2016) experiment in Brazil, are chosen to build the long-term statistics of SCM performance. In addition, a few 1-day cases are selected to use both SCMs and cloud-resolving models (CRMs) for detailed process understanding of model errors in DCP. The goal of this study is to document common model behaviors in simulating the diurnal cycle of precipitation in current weather and climate models by constraining the large-scale conditions in the SCM framework and to provide a benchmark for more in-depth follow-up studies. In particular, this paper will focus on the long-term statistics of the SCM simulations on DCP. More results on SCMs and CRMs for selected cases will be analyzed in a separate paper.

2. Experimental Design and Participating Models

2.1 Experimental Design

Two sets of SCM experiments are designed to build up statistics and connection to climate errors at two continental land locations using a series of short-range 5-day hindcast simulations. The first experiment spans twelve warm seasons (May – August) between 2004 to 2015 at the ARM SGP site. The second experiment is two full years from 2014 to 2015 at the ARM MAO site. The default protocol for the SCM simulations is a 5-day non-nudging hindcast, i.e., each SCM is initiated at 00Z every day and runs freely for 5 days without constraining temperature and moisture fields. Compared to typical SCM experiment protocols such as free run (e.g., Ghan et al. 2000) or nudging run, in the 5-day hindcast run the large-scale condition will not drift too far away, and SCM is expected to replicate similar model biases as in GCM (Bogenschutz et al. 2020), so that modelers can identify problems related to parameterizations using SCM hindcast run. In this study, the 24 – 48 hr simulations (day-2 hindcast) are used for analysis. In total there are 123 days (1 May to 31 August) per warm season at SGP and 361 days (2 January to 28 December since the 5-day simulations do not cross two years) per year at MAO to build the statistics.

SCMs are driven with the large-scale forcing derived from the constrained variational analysis (Zhang and Lin 1997; Zhang et al. 2001), which has been widely used in earlier GASS SCM intercomparison studies. The large-scale forcing data at SGP are from the ARM continuous forcing datasets at SGP (Xie et al. 2004; Tang et al. 2019), while the large-scale forcing at MAO are described in Tang et al. (2016). The initial conditions, surface latent and sensible heat fluxes, horizontal winds and the large-scale horizontal and vertical advections are all prescribed from the large-scale forcing data. Precipitation in the large-scale forcing data, which are from radar measurements averaged within a domain of ~300km in diameter at SGP and ~220km in diameter at MAO, is also used to evaluate model performance.

2.2 Participating Models

Participants in this intercomparison project submitted results from 11 SCMs with all required simulations at SGP and MAO. The basic information of these models is listed in Table 1, and more information about their deep convective parameterizations is listed in Table 2. Note that some of these models have an inheritance relationship with differences in model versions or physical parameterizations. For example, EAMv1 has two other versions: EAMv1.trigger and EAMv1.SILHS, with different deep convective schemes. EAMv1.trigger applies a modified convective trigger that was shown to significantly improve DCP (Xie et al. 2019); EAMv1.SILHS shuts off EAMv1's native deep convective scheme and lets the Cloud Layers Unified By Binormals scheme (CLUBB) treat both shallow and deep convection (Thayer-Calder et al. 2015; Guo et al. 2021), with a Subgrid Importance Latin Hypercube Sampler (SILHS, Larson and Schanen 2013) to interface clouds with microphysics on the subgrid scale. Moreover,

SCAM5 is the earlier version of SCAM6, and SAM0-UNICON is developed based on SCAM5 with a unified convection scheme (UNICON, Park 2014a, 2014b) for shallow and deep convection. Some models also perform simulations with different model setups or configurations for sensitivity studies. For example, SCAM6 and SKIM perform simulations with an interactive land model; SKIM submitted simulations with atmospheric states nudging to the observations. The variety of simulations allows us to test model sensitivity to parameterizations and model setup. Although models have different vertical and temporal resolution, they are all interpolated (or averaged) into 40 vertical levels and 1-hour resolution. The model data are archived and publicly available at <https://portal.nersc.gov/project/mp193/GASS/SCM/data/>.

3. Model Performances on the Mean Diurnal Cycle of Precipitation

3.1 General features

The two ARM sites are located in two distinct but representative environmental conditions: SGP represents typical mid-latitude land condition with upper-level westerlies and dry free troposphere; MAO represents typical tropical rain-forest condition with warm, moist air in the lower and middle troposphere. A set of diagnostic plots of the meteorological and process-level variables are made available at the GASS-DCP quick-plot webpage (https://portal.nersc.gov/project/mp193/GASS/SCM/quick_plots/). Due to the length limit, this paper only shows some of them that are closely related to DCP.

3.1.1 Mean diurnal cycle of precipitation

The mean DCP and the harmonic dial plots for the twelve summer seasons at SGP and the two years at MAO are shown in Figure 2. “Harmonic dial plot” (Covey et al. 2016) is a two-dimensional vector diagram in which the radius and angle represent the amplitude and phase, respectively, of the first component of Fourier analysis on the diurnal timeseries (sinusoidal function with period of 24 hours). The observed precipitation at SGP shows a nocturnal precipitation peak after midnight and a daytime minimum at around noon. The diurnal harmonic peak is at around 01 LST. Many models, such as EAMv1, SCAM6, SAM0-UNICON and SMCPCP, produce a precipitation peak during daytime, with harmonic phases between ~11 and 15 LST and amplitudes between 1 and 2 mm/day. The failure to produce a nocturnal precipitation peak at SGP is consistent with previous global model studies (e.g., Tang et al. 2021). ICON produces early-morning precipitation peak but its magnitude and diurnal amplitude are much lower than the observations. A few models produce a nocturnal precipitation peak, such as SKIM, CMC and TaiESM1. The mechanisms that help these models capturing nocturnal precipitation will be discussed later in Section 3.3.

The observed precipitation at MAO shows an early afternoon peak with the diurnal harmonic peak just after noon. The precipitation peak is stronger and smoother in the wet season, while it

is weaker and sharper in the dry season (Figure 3). Models have a spread in diurnal amplitude and phase, with precipitation amplitudes ranging from 1.5 to 6 mm/day and the diurnal phases occurring as early as 12 LST to as late as 17 LST. The diurnal phases in both observations and models are more similar in the dry season than in the wet season, while the precipitation amounts and amplitudes are larger in the wet season in observation and most models (Figure 3). Since DCP is affected by several types of convective systems that occur at different times of the day in both dry and wet seasons (e.g., Tang et al. 2016), we will focus on model performance for different types of convective systems instead of in different seasons.

3.1.2 Diurnal cycle of clouds

The observed cloud fractions at SGP and MAO both show a low-level cloud peak rising along with the daytime boundary layer development (Figure 4). The transition of shallow-to-deep convection has been extensively studied focusing on the following mechanisms: boundary layer turbulence strength, including boundary layer inhomogeneity (e.g., Zhang and Klein 2010) and cold pools from rain evaporation (e.g., Khairoutdinov and Randall 2006; Mapes and Neale 2011; Del Genio et al. 2012); and free troposphere humidity and instability, including the preconditioning from shallow convection via detrainment or dilution (e.g., Rio et al. 2009; Mapes and Neale 2011; Del Genio et al. 2012; de Rooy et al. 2013; Hohenegger and Stevens 2013; Ruppert and Johnson 2015; Zermeño-Díaz et al. 2015). Most of these studies used observations or idealized models, and only a few of them attempted to represent the transition in GCMs (Del Genio et al. 2012; Rio et al. 2013). Among the eight SCMs, SAM0-UNICON well captures the gradually rising of low clouds peak at both SGP and MAO; EAMv1 and SCAM6 capture the low clouds rising, although their low cloud fraction is underestimated at SGP; other models all fail to produce the rising low clouds in the daytime. This result reveals that capturing the development of shallow clouds and the transition from shallow to deep clouds is still a big challenge for current climate models. The encouraging results from using a unified scheme for turbulence and shallow (CLUBB) in EAMv1 and SCAM6 or a unified scheme for shallow and deep convection (UNICON) in SAM0-UNICON suggest the unified treatment of these processes could be one way to address this issue.. This is consistent with the findings in previous attempts of unified schemes such as in Frenkel et al. (2011a, 2011b), which used a simple multicloud model coupled to a bulk boundary layer scheme to simulate the diurnal cycle of tropical precipitation. For high clouds, most models overestimate high cloud fraction comparing to observations at SGP and MAO. The diurnal variation of high clouds is also poorly simulated at SGP but reasonably reproduced at MAO. Although model performances do behave differently at different locations, the differences of model-observation biases indicate the complexity to use one globally uniform parameterization to represent all environment conditions correctly.

3.1.3 Precipitation versus relative humidity

Previous studies have shown a relationship between precipitation and column-integrated relative humidity (CRH) in observations at daily (e.g., Bretherton et al. 2004) and sub-daily (e.g.,

Holloway and Neelin 2009; Neelin et al. 2009) timescales, although it should be noted that using CRH is an approximation for a more complex precipitation-moisture-temperature relationship (Kuo et al. 2018). How well models can capture the observed precipitation-CRH relationship is related to the representation of convection and its interaction with the large-scale environment, which provides insights to model improvements on convection and precipitation (e.g., Kuo et al. 2020). Here we examine the relationship of precipitation amount and frequency with CRH, as well as the occurrence frequency of each CRH bin (2% interval) in Figure 5. Observations show a strongly increasing relationship between precipitation amount and CRH at both sites. Precipitation picks up quickly and increases exponentially when CRH reaches 60% ~ 70% at SGP and 75% ~ 80% at MAO. Most models, except ICON, simulate higher (lower) precipitation probability (Figure 5 mid-row) and precipitation amount (Figure 5 top-row) compared to the observations when CRH is low (high). However, there are also more high-CRH days and less moderate-CRH days in these models than in observations (Figure 5 bottom-row). This indicates that models tend to produce light rainfall too easily in moderately dry conditions but have difficulties producing strong precipitation in wet conditions, although they are more likely to produce high CRH. This is consistent with the long-standing model error in GCMs that models rain too frequently at reduced intensity (Dai 2006; Sun et al. 2007; Stephens et al. 2010). In ICON, precipitation picks up at a much higher CRH. It also produces more wet conditions and less dry conditions than observations and other models. This may be related to the fact that ICON requires the whole box to be saturated for large-scale precipitation while other models allow partial cloudiness for microphysics. This would lead to a later onset of large-scale precipitation and higher relative humidity in ICON.

In the next two subsections, we select two convection regimes to further investigate the model biases on DCP: afternoon precipitation regime that is primarily surface-driven deep convection and nocturnal precipitation regime that is primarily associated with propagating MCSs and elevated convection. Based on observations, the afternoon precipitation days are selected by modifying the criteria of Zhang and Klein (2010). For SGP, an afternoon precipitation day is chosen when it has (1) peak rain rate greater than 1 mm/day, (2) rain peak time between 13 and 20 LST and (3) the peak rain rate 1.5 times greater than any rain rate outside of 13 to 20 LST. For MAO, an afternoon precipitation day is chosen when it has (1) peak rain rate greater than 1 mm/day, (2) rain peak time between 11 and 20 LST, (3) the peak rain rate 1.5 times greater than any rain rate outside of 11 to 20 LST, and (4) it must fall into the locally-driven convection case library visually selected from radar and satellite images (Tian et al. 2021). The last criterion is set to exclude those cases of propagating MCSs with a daytime rainfall peak, which occur frequently during the rainy season at MAO and overlap with locally generated rainfall (Tang et al. 2016). A nocturnal precipitation day at SGP and MAO is chosen when it has (1) peak rain rate greater than 1 mm/day, and (2) rain peak time between 00 and 07 LST. Overall, there are 136 and 380 days selected for the afternoon and nocturnal precipitation days, respectively, during the twelve warm seasons at SGP, and 111 and 73 days selected for the afternoon and nocturnal precipitation days, respectively, during the two years at MAO.

3.2 Afternoon Precipitation Regime

3.2.1 Diurnal cycle of precipitation

The mean diurnal cycle of total precipitation and convective precipitation fraction for the selected afternoon precipitation days at SGP and MAO are shown in Figure 6. Also shown are the harmonic dial plots of total precipitation. The observations show that the afternoon regime precipitation picks up after 09 LST at both sites, reaches a daily maximum around 17 LST at SGP and 14 LST at MAO, then decreases to late-night/early-morning values around 21 LST. In the diurnal harmonic analysis, the diurnal phase of afternoon precipitation at SGP is well captured in most SCMs, as opposed to the timeseries of all events in Figure 2, while their diurnal amplitudes vary. At MAO, models have a large spread of afternoon precipitation peak time, consistent with the timeseries of all events in Figure 2. EAMv1 shows large precipitation in the morning with the diurnal phase peak at noon; SMCP and SAM0-UNICON have a late afternoon peak just after 18 LST; SCAM6, SKIM and TaiESM1 capture the observed diurnal phase, but their diurnal amplitudes are much smaller. ICON produces two precipitation peaks, one in the morning and the other in the late afternoon, with much lower magnitude. The different model treatments of the preconditioning, triggering, developing of convection and convection interaction with environment via entrainment/detrainment may be responsible for the large spread or model performance. Another aspect is the presence of cold pool environments and associated boundary layer features and triggering of secondary developments, leading to the propagation as well as organization of convection (e.g., Oliveira et al. 2020). It is also likely that these processes are complex and location-dependent, so that effort is needed to improve the current globally uniform convective parameterization.

Figure 7 shows the frequency of diurnal maximum precipitation occurrence at each hour. The model performance of maximum precipitation frequency is consistent with their performance of mean DCP in Figure 6. The maximum diurnal precipitation occurs mostly between 15 – 19 LST at SGP and 13 – 17 LST at MAO, consistent with the time of large mean diurnal precipitation (Figure 6). Models generally capture the maximum precipitation time at SGP, with a few percentages of time when models produce maximum precipitation too early or too late. At MAO, models frequently produce maximum precipitation either too early or too late compared to observation, except SKIM. This again indicates that the response of model precipitation to environment at moist tropical land is not as sophisticated as at mid-latitude land.

3.2.2 Apparent heating and drying

In the daytime, all models produce most of their precipitation from convection, with convective precipitation fraction close to 100% (second row of Figure 6). The model performance of afternoon convection is further examined by looking at the vertical profiles of apparent heating (Q_1) and drying (Q_2) in Figure 8. Q_1 and Q_2 were first introduced by Yanai et al. (1973) to estimate the diabatic processes:

$$Q_1 = \frac{1}{c_p} \left(\frac{\partial \bar{s}}{\partial t} + \bar{\vec{V}} \cdot \nabla \bar{s} + \bar{\omega} \frac{\partial \bar{s}}{\partial p} \right) = \frac{1}{c_p} \left(Q_{rad} + L_v(d_w + d_i) - \frac{\partial \bar{\omega}'s'}{\partial p} \right) \quad (1)$$

$$Q_2 = -\frac{L_v}{c_p} \left(\frac{\partial \bar{q}}{\partial t} + \bar{\vec{V}} \cdot \nabla \bar{q} + \bar{\omega} \frac{\partial \bar{q}}{\partial p} \right) = \frac{L_v}{c_p} \left(d_w + d_i + \frac{\partial \bar{\omega}'q'}{\partial p} \right) \quad (2)$$

where $s = C_p T + gz$ is the dry static energy and C_p is the specific heat for dry air in constant pressure; q is water vapor mixing ratio; \vec{V} is horizontal wind vector; ω is vertical velocity in pressure coordinate; Q_{rad} is radiative heating; $L_v(d_w + d_i)$ is the latent heat from liquid and ice processes; the overbar refers to a horizontal average and the prime refers to a deviation from the average. The “observed” Q_1 and Q_2 are derived from the large-scale dynamics (the center part of the equations) from the variational analysis while the “simulated” Q_1 and Q_2 are the sum of all physical tendencies in the model (the right-hand-side of the equations). The simulated vertical profiles of Q_1 and Q_2 are generally consistent with observations at SGP (Figure 8, left column), with heating peak in the middle to upper troposphere around 400 to 500 hPa. However, there are large discrepancies of Q_1 and Q_2 profiles at MAO (Figure 8, right column). Models produce a heating peak near 700 to 800 hPa, much lower than the observed peak at near 500 hPa. While the observed heating remains large to about 150 mb, model heating is small about 500 mb. They also fail to reproduce the observed moisture sink between 250 and 650 hPa. These discrepancies were also found in Large Scale Biosphere–Atmosphere Experiment (LBA) conducted in Southwest Amazonia (Ma et al. 2021a), indicating that models produce too shallow afternoon convection over the broad Amazon region. The fact that models simulate Q_1 and Q_2 well at SGP but poorly at MAO also highlights the dependence of model performances at different locations. The poor performance at deep convection at MAO despite being driven by observed large-scale forcing suggests significant common deficiencies in deep convective parameterization over tropical land.

3.2.3 Deep convection triggering

At both SGP and MAO, a common model bias in DCP is the early onset of precipitation. The observed diurnal precipitation at both SGP and MAO picks up quickly near 12 LST, while many models produce notable precipitation a few hours earlier (Figure 6). To further quantify the early onset of precipitation, we define the precipitation onset time as the first hour after 06 LST when the precipitation at that hour increases above 1 mm/day. The statistics of precipitation onset time are shown in Figure 9. The models we are discussing in this section are shown in thick lines, and those will be discussed in Section 4 for sensitivity study are shown in thin lines. The mean onset time of precipitation is observed in early afternoon at SGP and around noon at MAO, about 3-4 hours earlier than the maximum precipitation time (Figure 7). However, the SCM-simulated onset time is usually 1 to 2 hours earlier than in observations at SGP, and up to 4 hours earlier at MAO, even for those models produce maximum precipitation in a later time (Figure 7). CMC and ICON have a consistent mean precipitation onset time with observation at MAO, but their diurnal distribution is broader, with three (CMC) or two (ICON) precipitation peaks during the daytime (top right panel of Figure 6).

Among these SCMs, EAMv1, SCAM6, SMCP CP and ICON use CAPE to trigger deep convection (Table 2). This CAPE-based convective trigger is believed to trigger convection too easily and too frequently (e.g., Xie and Zhang 2000; Ma et al. 2021b). A modified trigger using dynamic CAPE (dCAPE) introduced by Xie and Zhang (2000) and further enhanced in Xie et al. (2019) is implemented in EAMv1.trigger and show promising results on mitigating the early onset of convection (see further discussion in Section 4). Using a CIN-based convective trigger, SKIM shows good precipitation onset time at SGP, but too early onset time at MAO, possibly due to the low-CIN environment in the Amazon permitting convection to trigger too easily but not through a sufficient deep layer.

Another well-known issue of early onset of deep convection in GCMs is the poor simulation of the transition of shallow-to-deep convection and the gradual moistening of the free troposphere (Guichard et al. 2004; Zhang and Klein 2010). Shallow and deep convection is usually related to very different forcing regimes, entrainment and detrainment rates, and environment conditions. Therefore, almost all previous GCMs separate them into different schemes, and they work reasonably well in practice. However, separating the two schemes usually leads to an overly abrupt transition from one condition to another (e.g., Rio et al. 2009). Deep convection is often triggered as soon as the large-scale environment reaches the triggering criterion in the model, instead of developing through an intermittent stage of preconditioning of the free atmosphere as in the real world. SAM0-UNICON uses a new parameterization that aims to unify shallow and deep convective schemes to simulate the complex interactions between subgrid and grid-scale processes such as the transition from shallow to deep convection. While it correctly simulates the precipitation onset time at SGP, at MAO it encounters similar deficiency of ~2 hr earlier onset time (Figure 9). It may be partly related with the inability of SCM to handle horizontal advection of subgrid cold pools. This reveals a major challenge in unified parameterization to treat all conditions within a single set of equations and a need to test the models in global simulations.

3.3 Nocturnal Precipitation Regime

3.3.1 Diurnal cycle of precipitation

The mean diurnal cycle of total precipitation, convective precipitation fraction and the diurnal harmonic dial plots of total precipitation for nocturnal precipitation days are shown in Figure 10. Nocturnal precipitation is typically related to the elevated convection above nocturnal stable boundary layer (e.g., Lee et al. 2008; Geerts et al. 2017) or propagating MCSs. The observations show a diurnal peak at ~03 LST at SGP and ~05 LST at MAO, with a diurnal peak of ~20 mm/day and harmonic amplitude of ~8 mm/day, much larger than the afternoon precipitation events in Figure 6. At 12~15 LST, precipitation at SGP reaches its diurnal minimum, while precipitation at MAO reaches a secondary peak, close to but, weaker than the peak of afternoon precipitation. This indicates that even when the nocturnal precipitation has released some instability of the atmosphere, the solar heating in the following daytime and the moist environment can still trigger afternoon convection.

From Figure 10, SCMs can be divided into two groups in simulating nocturnal precipitation at SGP. SKIM, CMC and TaiESM1 well capture the diurnal phase and amplitude of nocturnal precipitation, and ICON also captures the diurnal phase but underestimates the amplitude of nocturnal precipitation. EAMv1, SCAM6, SAM0-UNICON and SMCPCP produce diurnal precipitation later with smaller magnitude. The models that well capture nocturnal precipitation at SGP also perform well at MAO, while the other models produce either a smaller magnitude or later phase of DCP. Between 00 and 06 LST, SKIM, CMC, TaiESM1 and ICON produce most of their precipitation (70% – 90%) from the convective parameterization at both sites, while other models produce ~60% of their precipitation at SGP and 40% – 95% of their precipitation at MAO as large-scale precipitation. Although impacted by convective process such as latent heating and detrainment, the large-scale precipitation produced in SCMs is primarily attributed to the prescribed large-scale forcing, which is constrained by the observed surface precipitation. In free-run GCMs, where the large-scale forcing interacts with model physics and is affected by their deficiencies, the simulation of nocturnal precipitation could be even worse (e.g., Tang et al. 2021). Thus, it seems to be necessary to improve the deficiencies in model parameterizations found in the present study that might potentially contribute to model errors in a less constrained model setup.

There is a distinguishing feature that separates these two groups of models: whether or not the model allows elevated convection triggered above the boundary layer. EAMv1, SCAM6 and SMCPCP all use the ZM deep convective scheme with the launching parcel chosen only within the boundary layer. SKIM and TaiESM1 select air parcels below ~700 hPa ($\sigma=0.7$) and 600 hPa, respectively, and ICON selects air parcels within 350hPa above the surface. It is natural to hypothesize that allowing convection to occur above the boundary layer is the key to simulate nocturnal convection. In the sensitivity study in Section 4, when the default ZM scheme is modified by unlimiting the launching level, the nocturnal precipitation in EAMv1.trigger is significantly improved compared to default EAMv1. CMC has a separated mid-level convective scheme to capture elevated convection (McTaggart-Cowan et al. 2020). The mid-level scheme exhibits a maximum activity during the night (Figure 11). However, its contribution to the total precipitation is very modest while deep convection contributes the most for nocturnal precipitation. Further sensitivity tests with different thresholds for deep and mid-level convection triggering have shown little sensitivity of the phase of DCP to how active the deep and mid-level schemes are.

3.3.2 Apparent heating and drying

Figure 12 shows the 00-06 LST mean vertical profiles of Q_1 and Q_2 at SGP and MAO for the nocturnal precipitation events. The observed heating profile is top-heavy at SGP and roughly parabolic at MAO, showing typical convective conditions over mid-latitude continent and tropics, respectively. The condensational drying has a sharper and stronger peak at MAO than SGP. It is interesting to see that all models produce heating and drying peaks at a similar height to that of the observed, despite their wide ranges of convective fraction as shown in Figures 6

and 10 (e.g., Schumacher et al. 2004). The reasonable simulation of nocturnal convective heating depth at MAO (Figure 12b) is notable given the poor performance at afternoon convective heating depth (Figure 8b), possibly related to that, afternoon convection is locally-driven while nocturnal convection is propagating organized convection. The magnitude of Q_1 and Q_2 varies among models. SKIM, TaiESM1 and CMC produce similar magnitudes of Q_1 and Q_2 comparable with observations, while the other models produce smaller magnitudes (except ICON Q_1 at MAO). The reduction of the Q_1 peak in these models is more prevalent in the upper levels, which may be related to the weaker convective activity that is not sufficient to remove all the instability from the large-scale forcing. The remaining instability in these models is then released at a later time, causing the morning-time precipitation peak seen in Figure 10.

4. Sensitivity Study

In addition to the default simulations, some modeling centres also performed other simulations using different model versions, physical schemes or configurations. Table 3 shows the information of the simulations included in this section emphasizing their differences from the default models/runs. DCP in SKIM.nudge is very similar to the default runs, so we choose not to show them to make the figures more readable. Moreover, SAM0-UNICON is included in this sensitivity study because of two reasons: firstly, it is developed from SCAM5, with the same turbulence, microphysics and macrophysics schemes but a different convective scheme; secondly, it unifies shallow and deep convection, so we feel it is interesting to compare it with another model with unified shallow and deep convection (EAMv1.SILHS).

Figure 13 shows DCP performance of the models for sensitivity study in the afternoon precipitation regime, while Figure 14 shows DCP performance in the nocturnal precipitation regime. EAMv1.trigger uses a modified convective trigger, which uses a dynamic CAPE (dCAPE: CAPE changes due to large-scale advections) to trigger convection and allow air parcels to launch above the boundary layer. The improvement of DCP in GCMs has been demonstrated in Xie et al. (2019), Wang et al. (2020) and Cui et al. (2021). Here for SCM, the improvement of DCP is also shown at SGP and MAO (Figures 13 and 14) (blue dashed line and open circle). We believe that the dCAPE trigger helps delay the precipitation onset of afternoon precipitation while allowing air parcels to launch above the boundary layer helps convection occur at night.

Another independent modification of EAMv1, EAMv1.SILHS, also shows significant improvement on DCP in the two precipitation regimes. Instead of using ZM for deep convection and CLUBB for shallow convection and large-scale clouds and precipitation in the default EAMv1, EAMv1.SILHS uses CLUBB for all shallow convection, deep convection and large-scale clouds and precipitation. Therefore, the convective fraction is zero because it does not separate convective and large-scale precipitation. The CLUBB is interfaced to the microphysics

scheme using the subgrid sampler SILHS. It well captures the elevated convection at night as shown in Figure 14, possibly because it does not need a convective trigger nor specification of parcel launching level. For afternoon precipitation, it delays the precipitation onset time on both SGP and MAO (Figure 9), but only produces about half of the observed peak precipitation and ~30% of the harmonic amplitude (Figure 13). This is subject to further improvements.

Another model with a unified convective scheme, SAM0-UNICON, is also shown in Figures 13 and 14. Note that SAM0-UNICON and SCAM6 both have a tight relationship with SCAM5: SAM0-UNICON has the same turbulence, microphysics and macrophysics schemes as SCAM5, but a different shallow and deep convective scheme. SCAM6 only shares the same deep convective scheme with SCAM5, with turbulence, shallow convection and macrophysics replaced by CLUBB. The DCP performance in SCAM6 is similar as in SCAM5, while SAM0-UNICON shows larger differences with SCAM5. This indicates that DCP is primarily controlled by the deep convective scheme. Since SAM0-UNICON can simulate the complex interactions between subgrid and grid-scale processes such as the transition from shallow to deep convection, it captures well the afternoon precipitation, especially at SGP. However, its performance on nighttime precipitation still needs to be improved. This is consistent with previous work in global simulations (Park 2014b; Tang et al. 2021).

Two models conducted sensitivity tests with an interactive land model. SCAM6 is coupled with the community land model version 5.0 (CLM5, Lawrence et al. 2019), while SKIM is coupled with the revised Noah land surface model version 3.4.1 (Koo et al. 2017). SKIM.land performs similar to the default SKIM run, while SCAM6.land performs better than SCAM6, with the early onset of afternoon precipitation (see Figure 9 and Figure 13) and the morning rainfall in nocturnal precipitation days (Figure 14) both reduced. It is interesting to see that SCAM6.land produces much lower latent heat fluxes and higher sensible heat fluxes than observations (Figure 15). The estimated ground heat flux is also much larger in SCAM6.land than in other models, with daily mean of 61.7 W/m^2 at SGP and 59.0 W/m^2 at MAO. The corresponding ground heat flux in SCAM6 is -9.4 W/m^2 at SGP and -3.9 W/m^2 at MAO, and that in the observations is 4.9 W/m^2 at SGP and -5.3 W/m^2 at MAO. On the other hand, SKIM.land also produces lower latent heat fluxes and higher sensible heat fluxes than observations, likely due to more humid near-surface air or misrepresented surface conditions such as vegetation fraction, land type or soil properties. Its turbulent flux errors are smaller than SCAM6.land, and its ground heat flux is similar with SKIM and observations. Despite the differences in the land models used in SCAM6.land and SKIM.land, it may be inferred that the land-atmospheric interactions in climate models are not well represented so that a model (SCAM6.land) needs to produce more unrealistic surface fluxes in order to get more realistic precipitation in deep convective regimes.

5. Summary and Discussions

The diurnal cycle of precipitation (DCP) is a problem that GCMs have struggled to represent in past decades (Fiedler et al. 2020). Although the latest GCMs in the recent CMIP6 have shown improvement in simulating DCP (Tang et al. 2021), they still suffer from the persistent problems of too early precipitation and missing nocturnal precipitation.

The GEWEX Global Atmospheric System Study (GASS) Panel organized a project focusing on understanding and improving the model capability to simulate diurnal precipitation phenomena through multi-model intercomparison studies against observations. This study focuses on the intercomparison of SCMs to understand what processes control the diurnal cycle of precipitation over different climate regimes and identify the deficiencies and missing physics in current model parameterizations. Instead of focusing on a particular intensive observing period for several days to a few months as in previous SCM intercomparison studies, we have performed long-term hindcast simulations to obtain robust statistics of model performances on DCP. Eleven SCMs from different modeling centers around the world have participated in this project.

DCP in twelve summer seasons at a midlatitude land site (SGP) and two continuous years at a tropical land site (MAO) are investigated in this study. The two selected sites have distinguished and representative characteristics of the large-scale environment, clouds and precipitation. The participating SCMs do not always show the same discrepancies at the two sites. This indicates that some parameterization assumptions may not work well across all climate regimes.

Two regimes of DCP are examined in this study, one is surface-driven afternoon convection and the other is nocturnal precipitation caused by elevated convection or propagating convective systems. For afternoon convection, precipitation in most SCMs initiated 1 to 4 hours earlier than observation. The early onset of precipitation is more severe at MAO than at SGP. It appears to be associated with two other issues common across all the models for MAO afternoon precipitation cases: a severe deficiency of convective heating in the upper troposphere, and rainfall too evenly spread across times of day. In other words for the MAO afternoon cases, models fail to develop strong deep convection but precipitate too easily from convection in the lower troposphere. At SGP, the early onset of afternoon precipitation may be due to the missing transition of shallow-to-deep convection in climate models. More sophisticated parameterizations that unify shallow and deep convection (e.g., UNICON, CLUBB-SILHS) can improve the early onset problem, although UNICON shows more deficiencies in the precipitation-CRH relationship. For nocturnal precipitation, although all SCMs produce considerable precipitation at night, the partitioning of convective precipitation and large-scale precipitation differ dramatically among models. Models with most of the nocturnal precipitation generated from large-scale are likely driven by the prescribed large-scale forcing. SCMs that produce most of nocturnal precipitation from convection (SKIM, TaiESM1, CMC, ICON and EAMv1.trigger) all allow convection to be triggered above the boundary layer. Although a few recent studies have considered convection moving across grids (Malardel and Bechtold 2019; McTaggart-Cowan et al. 2019b), most SCMs and their parent GCMs still struggle to propagate convection from one grid to another. The

574 capability to detect mid-level instability above the boundary layer is important for them to
575 simulate nocturnal precipitation.

576 Sensitivity studies were performed using continuous nudging runs, different parameterizations,
577 or interactive land models. Using a revised convective trigger specifically targeting improvement
578 on the diurnal cycle of precipitation, EAMv1.trigger shows the importance of dynamically
579 constraining the convective trigger and allowing parcels to launch above the boundary layer in
580 traditional convective parameterizations to produce precipitation at the right time. The
581 representation of shallow convection phase and its transition to deep convection is still a key
582 aspect to be improved in models. One path towards improving this feature is the effort of
583 unifying shallow and deep convection, as seen in SAM0-UNICON and EAMv1.SILHS. On the
584 other hand, in the two land-atmosphere coupled simulations, the one with larger biases in surface
585 turbulent fluxes (SCAM6.land) shows more improvement on DCP. This indicates that the
586 relationship between the land-atmospheric interaction and DCP is complicated and points to the
587 importance of the representation of boundary-layer processes in deep convective regimes.
588 Further study is needed to investigate how the representation of land-atmospheric coupling will
589 influence simulation of DCP.

590 Although not the focus of this study here, the discrepancy in the amplitude of DCP should also
591 be pointed out. In addition to deep and shallow convection, boundary layer processes can highly
592 contribute to the control of the diurnal amplitude (e.g., Koo and Hong 2010). Therefore, a
593 diversity of turbulence schemes (Table 1) might be a source of large spread in diurnal amplitude,
594 which needs to be addressed in future study.

595 This SCM intercomparison study provides insights of which physical processes are essential in
596 climate models to simulate DCP, given a large-scale environment close to the real world. In a
597 global or regional model, the model biases in large-scale dynamic and thermodynamic states and
598 the interactions between the large-scale fields and physics also impact the simulation of DCP.
599 This is not revealed in the SCM study. An intercomparison of global and regional climate models
600 is currently underway and more details will be presented on DCP over broader regions in the
601 near future.

602 603 *Acknowledgement:*

604 *This work is part of The GEWEX Global Atmospheric System Study (GASS) Panel's Diurnal*
605 *Cycle of Precipitation Project. Work at LLNL is supported by the Earth and Environmental*
606 *System Modeling, Regional and Global Model Analysis, Atmospheric System Research and*
607 *Atmospheric Radiation Measurement programs, funded by the U.S. Department of Energy,*
608 *Office of Science, Office of Biological and Environmental Research, and performed under the*
609 *auspices of the U.S. DOE by Lawrence Livermore National Laboratory under Contract DE-*
610 *AC52-07NA27344. S. Tang was partially supported by the "Enabling Aerosol-cloud interactions*
611 *at GLocal convection-permitting scales (EAGLES)" project (74358) funded by the U.S.*

612 *Department of Energy, Office of Science, Office of Biological and Environmental Research,*
613 *Earth System Model Development program. Pacific Northwest National Laboratory (PNNL) is*
614 *operated for DOE by Battelle Memorial Institute under contract DE-AC05-76RL01830. J. D.*
615 *Neelin was supported by NSF project AGS-1936810.*
616

Appendix: Model schemes and abbreviations in Tables 1, 2 and 3

Bechtold14: convective scheme from Bechtold et al. (2014)
CAPE: convective available potential energy
CIN: convective inhibition
CLUBB: Cloud Layers Unified By Binormals (Golaz et al. 2002; Larson and Golaz 2005; Larson 2017)
dCAPE: dynamic CAPE generation rate from large-scale tendency (Xie and Zhang 2000)
UW-diag_TKE: University of Washington diagnostic turbulent kinetic energy scheme (Bretherton and Park 2009)
GTS: Global Forecast System (GFS) – Taiwan Earth System Model (TaiESM) – Sundqvist scheme (Shiu et al. 2021)
HanPan: shallow convection from Han and Pan (2011)
HB: turbulent scheme from Holtslag and Boville (1993)
Köhler20: cloud cover parameterization from Köhler (2020)
KSAS: Korean Integrated Model (KIM, Hong et al. 2018) version of the simplified Arakawa-Schubert deep convection scheme (Han et al. 2020)
LCL: lifting condensation level
LFC: level of free convection
M-Bechtold: modified from Bechtold et al. (2001) (McTaggart-Cowan et al. 2019a)
MG: bulk two-moment cloud microphysics (Morrison and Gettelman 2008)
MG2: version 2 of MG microphysics (Gettelman et al. 2015)
Modified KF: modified from Kain and Fritsch (1990) (McTaggart-Cowan et al. 2019a)
Park1: macrophysics from (Park et al. 2014)
Park2: macrophysics from (Park et al. 2017)
PCH16: macrophysics from (Park et al. 2016)
UW-PB09: University of Washington shallow convective scheme (Park and Bretherton 2009)
PBL: planetary boundary layer
Raschendorfer00: turbulence scheme from Raschendorfer (2000)
Seifert08: single moment microphysics from Seifert (2008)
Shin-Hong: turbulence scheme from Shin and Hong (2015) with revision of Lee et al. (2018)
SILHS: Subgrid Importance Latin Hypercube Sampler (Thayer-Calder et al. 2015; Griffin and Larson 2016)
Sundqvist: microphysics from Sundqvist et al. (1989)
TKE1.5: 1.5 order turbulent kinetic energy scheme from McTaggart-Cowan et al. (2019a)
UNICON: Unified convective scheme (Park 2014a, 2014b)
Unified stochastic Plume-ZM: Unified Stochastic Mass-flux Cumulus integrated in ZM scheme (Khouider and Leclerc 2019)
WSM5: the Weather Research and Forecasting (WRF) single-moment 5-class microphysics scheme (Hong et al. 2004; Bae et al. 2016; Kim and Hong 2018)
ZM: Zhang-McFarlane convective scheme (Zhang and McFarlane 1995)

658 References:

- 659 Bae, S. Y., S.-Y. Hong, and K.-S. S. Lim, 2016: Coupling WRF Double-Moment 6-Class
660 Microphysics Schemes to RRTMG Radiation Scheme in Weather Research Forecasting Model.
661 *Advances in Meteorology*, **2016**, 5070154, 10.1155/2016/5070154.
- 662 Bašták Ďurán, I., and Coauthors, 2021: The ICON Single-Column Mode. *Atmosphere*, **12**, 906,
663 10.3390/atmos12070906.
- 664 Bechtold, P., and Coauthors, 2000: A GCSS model intercomparison for a tropical squall line
665 observed during toga-coare. II: Intercomparison of single-column models and a cloud-resolving
666 model. *Q. J. R. Meteorol. Soc.*, **126**, 865-888, 10.1002/qj.49712656405.
- 667 Bechtold, P., E. Bazile, F. Guichard, P. Mascart, and E. Richard, 2001: A mass-flux convection
668 scheme for regional and global models. *Q. J. R. Meteorol. Soc.*, **127**, 869-886,
669 10.1002/qj.49712757309.
- 670 Bechtold, P., J.-P. Chaboureau, A. Beljaars, A. K. Betts, M. Köhler, M. Miller, and J.-L.
671 Redelsperger, 2004: The simulation of the diurnal cycle of convective precipitation over land in
672 a global model. *Q. J. R. Meteorol. Soc.*, **130**, 3119-3137, 10.1256/qj.03.103.
- 673 Bechtold, P., and Coauthors, 2008: Advances in simulating atmospheric variability with the
674 ECMWF model: From synoptic to decadal time-scales. *Q. J. R. Meteorol. Soc.*, **134**, 1337-1351,
675 10.1002/qj.289.
- 676 Bechtold, P., N. Semane, P. Lopez, J.-P. Chaboureau, A. Beljaars, and N. Bormann, 2014:
677 Representing Equilibrium and Nonequilibrium Convection in Large-Scale Models. *J. Atmos.*
678 *Sci.*, **71**, 734-753, 10.1175/jas-d-13-0163.1.
- 679 Betts, A. K., and C. Jakob, 2002: Study of diurnal cycle of convective precipitation over
680 Amazonia using a single column model. *J. Geophys. Res. Atmos.*, **107**, ACL 25-1-ACL 25-13,
681 10.1029/2002jd002264.
- 682 Bogenschutz, P. A., S. Tang, P. M. Caldwell, S. Xie, W. Lin, and Y. S. Chen, 2020: The E3SM
683 version 1 single-column model. *Geosci. Model Dev.*, **13**, 4443-4458, 10.5194/gmd-13-4443-
684 2020.
- 685 Bretherton, C. S., S. K. Krueger, M. C. Wyant, P. Bechtold, E. Van Meijgaard, B. Stevens, and J.
686 Teixeira, 1999: A GCSS Boundary-Layer Cloud Model Intercomparison Study Of The First
687 Astex Lagrangian Experiment. *Bound.-Layer Meteorol.*, **93**, 341-380,
688 10.1023/A:1002005429969.
- 689 Bretherton, C. S., M. E. Peters, and L. E. Back, 2004: Relationships between Water Vapor Path
690 and Precipitation over the Tropical Oceans. *J. Climate*, **17**, 1517-1528, 10.1175/1520-
691 0442(2004)017<1517:Rbwvpa>2.0.Co;2.
- 692 Bretherton, C. S., and S. Park, 2009: A New Moist Turbulence Parameterization in the
693 Community Atmosphere Model. *J. Climate*, **22**, 3422-3448, 10.1175/2008JCLI2556.1.
- 694 Covey, C., and Coauthors, 2016: Metrics for the Diurnal Cycle of Precipitation: Toward Routine
695 Benchmarks for Climate Models. *J. Climate*, **29**, 4461-4471, 10.1175/jcli-d-15-0664.1.
- 696 Cui, Z., G. J. Zhang, Y. Wang, and S. Xie, 2021: Understanding the Roles of Convective Trigger
697 Functions in the Diurnal Cycle of Precipitation in the NCAR CAM5. *J. Climate*, **34**, 6473-6489,
698 10.1175/jcli-d-20-0699.1.
- 699 Dai, A., K. E. Trenberth, and T. R. Karl, 1999: Effects of Clouds, Soil Moisture, Precipitation,
700 and Water Vapor on Diurnal Temperature Range. *J. Climate*, **12**, 2451-2473, 10.1175/1520-
701 0442(1999)012<2451:Eocsmv>2.0.Co;2.

Dai, A., 2006: Precipitation Characteristics in Eighteen Coupled Climate Models. *J. Climate*, **19**, 4605-4630, 10.1175/jcli3884.1.

Davies, L., and Coauthors, 2013: A single-column model ensemble approach applied to the TWP-ICE experiment. *J. Geophys. Res. Atmos.*, **118**, 6544-6563, 10.1002/jgrd.50450.

de Rooy, W. C., and Coauthors, 2013: Entrainment and detrainment in cumulus convection: an overview. *Q. J. R. Meteorol. Soc.*, **139**, 1-19, 10.1002/qj.1959.

Del Genio, A. D., 2012: Representing the Sensitivity of Convective Cloud Systems to Tropospheric Humidity in General Circulation Models. *Surveys in Geophysics*, **33**, 637-656, 10.1007/s10712-011-9148-9.

Del Genio, A. D., Y. Chen, D. Kim, and M.-S. Yao, 2012: The MJO Transition from Shallow to Deep Convection in CloudSat/CALIPSO Data and GISS GCM Simulations. *J. Climate*, **25**, 3755-3770, 10.1175/jcli-d-11-00384.1.

Eyring, V., S. Bony, G. A. Meehl, C. A. Senior, B. Stevens, R. J. Stouffer, and K. E. Taylor, 2016: Overview of the Coupled Model Intercomparison Project Phase 6 (CMIP6) experimental design and organization. *Geosci. Model Dev.*, **9**, 1937-1958, 10.5194/gmd-9-1937-2016.

Fiedler, S., and Coauthors, 2020: Simulated Tropical Precipitation Assessed across Three Major Phases of the Coupled Model Intercomparison Project (CMIP). *Mon. Weather Rev.*, **148**, 3653-3680, 10.1175/mwr-d-19-0404.1.

Frenkel, Y., B. Khouider, and A. J. Majda, 2011a: Simple Multicloud Models for the Diurnal Cycle of Tropical Precipitation. Part I: Formulation and the Case of the Tropical Oceans. *J. Atmos. Sci.*, **68**, 2169-2190, 10.1175/2011jas3568.1.

———, 2011b: Simple Multicloud Models for the Diurnal Cycle of Tropical Precipitation. Part II: The Continental Regime. *J. Atmos. Sci.*, **68**, 2192-2207, 10.1175/2011jas3600.1.

Geerts, B., and Coauthors, 2017: The 2015 Plains Elevated Convection at Night Field Project. *Bull. Amer. Meteor. Soc.*, **98**, 767-786, 10.1175/bams-d-15-00257.1.

Gettelman, A., H. Morrison, S. Santos, P. Bogenschutz, and P. M. Caldwell, 2015: Advanced Two-Moment Bulk Microphysics for Global Models. Part II: Global Model Solutions and Aerosol-Cloud Interactions. *J. Climate*, **28**, 1288-1307, 10.1175/jcli-d-14-00103.1.

Gettelman, A., J. E. Truesdale, J. T. Bacmeister, P. M. Caldwell, R. B. Neale, P. A. Bogenschutz, and I. R. Simpson, 2019: The Single Column Atmosphere Model Version 6 (SCAM6): Not a Scam but a Tool for Model Evaluation and Development. *J. Adv. Model. Earth Syst.*, **11**, 1381-1401, 10.1029/2018ms001578.

Ghan, S., and Coauthors, 2000: A comparison of single column model simulations of summertime midlatitude continental convection. *J. Geophys. Res. Atmos.*, **105**, 2091-2124, 10.1029/1999JD900971.

Golaz, J.-C., V. E. Larson, and W. R. Cotton, 2002: A PDF-Based Model for Boundary Layer Clouds. Part I: Method and Model Description. *J. Atmos. Sci.*, **59**, 3540-3551, 10.1175/1520-0469(2002)059<3540:apbmfb>2.0.co;2.

Griffin, B. M., and V. E. Larson, 2016: Parameterizing microphysical effects on variances and covariances of moisture and heat content using a multivariate probability density function: a study with CLUBB (tag MVCS). *Geosci. Model Dev.*, **9**, 4273-4295, 10.5194/gmd-9-4273-2016.

Guichard, F., and Coauthors, 2004: Modelling the diurnal cycle of deep precipitating convection over land with cloud-resolving models and single-column models. *Q. J. R. Meteorol. Soc.*, **130**, 3139-3172, 10.1256/qj.03.145.

Guo, Z., B. M. Griffin, S. Domke, and V. E. Larson, 2021: A parameterization of turbulent dissipation and pressure damping time scales in stably stratified inversions, and its effects on low

clouds in global simulations. *J. Adv. Model. Earth Syst.*, **n/a**, e2020MS002278, 10.1029/2020MS002278.

Han, J.-Y., S.-Y. Hong, and Y. C. Kwon, 2020: The Performance of a Revised Simplified Arakawa–Schubert (SAS) Convection Scheme in the Medium-Range Forecasts of the Korean Integrated Model (KIM). *Weather and Forecasting*, **35**, 1113–1128, 10.1175/waf-d-19-0219.1.

Han, J., and H.-L. Pan, 2011: Revision of Convection and Vertical Diffusion Schemes in the NCEP Global Forecast System. *Weather and Forecasting*, **26**, 520–533, 10.1175/waf-d-10-05038.1.

Hohenegger, C., and B. Stevens, 2013: Preconditioning Deep Convection with Cumulus Congestus. *J. Atmos. Sci.*, **70**, 448–464, 10.1175/jas-d-12-089.1.

Holloway, C. E., and J. D. Neelin, 2009: Moisture Vertical Structure, Column Water Vapor, and Tropical Deep Convection. *J. Atmos. Sci.*, **66**, 1665–1683, 10.1175/2008jas2806.1.

Holtzlag, A. A. M., and B. A. Boville, 1993: Local Versus Nonlocal Boundary-Layer Diffusion in a Global Climate Model. *J. Climate*, **6**, 1825–1842, 10.1175/1520-0442(1993)006<1825:Lvnbl>2.0.Co;2.

Hong, S.-Y., J. Dudhia, and S.-H. Chen, 2004: A Revised Approach to Ice Microphysical Processes for the Bulk Parameterization of Clouds and Precipitation. *Mon. Weather Rev.*, **132**, 103–120, 10.1175/1520-0493(2004)132<0103:Aratim>2.0.Co;2.

Hong, S.-Y., and Coauthors, 2013: The Global/Regional Integrated Model system (GRIMs). *Asia. Pac. J. Atmos. Sci.*, **49**, 219–243, 10.1007/s13143-013-0023-0.

Hong, S.-Y., and Coauthors, 2018: The Korean Integrated Model (KIM) System for Global Weather Forecasting. *Asia. Pac. J. Atmos. Sci.*, **54**, 267–292, 10.1007/s13143-018-0028-9.

Jensen, M. P., and Coauthors, 2016: The Midlatitude Continental Convective Clouds Experiment (MC3E). *Bulletin of the American Meteorological Society*, **97**, 1667–1686, 10.1175/bams-d-14-00228.1.

Kain, J. S., and J. M. Fritsch, 1990: A One-Dimensional Entraining/Detraining Plume Model and Its Application in Convective Parameterization. *J. Atmos. Sci.*, **47**, 2784–2802, 10.1175/1520-0469(1990)047<2784:Aodepm>2.0.Co;2.

———, 1992: The role of the convective “trigger function” in numerical forecasts of mesoscale convective systems. *Meteorol. Atmos. Phys.*, **49**, 93–106, 10.1007/BF01025402.

Khairoutdinov, M., and D. Randall, 2006: High-Resolution Simulation of Shallow-to-Deep Convection Transition over Land. *J. Atmos. Sci.*, **63**, 3421–3436, 10.1175/jas3810.1.

Khouider, B., and E. Leclerc, 2019: Toward a Stochastic Relaxation for the Quasi-Equilibrium Theory of Cumulus Parameterization: Multicloud Instability, Multiple Equilibria, and Chaotic Dynamics. *J. Adv. Model. Earth Syst.*, **11**, 2474–2502.

Khouider, B., B. Goswami, R. Phani, and A. Majda, 2021: A shallow-deep unified stochastic mass-flux cumulus parameterization in the single column Community Climate Model. *J. Adv. Model. Earth Syst.*, Under Review.

Kim, S.-Y., and S.-Y. Hong, 2018: The Use of Partial Cloudiness in a Bulk Cloud Microphysics Scheme: Concept and 2D Results. *J. Atmos. Sci.*, **75**, 2711–2719, 10.1175/jas-d-17-0234.1.

Klein, S. A., and Coauthors, 2009: Intercomparison of model simulations of mixed-phase clouds observed during the ARM Mixed-Phase Arctic Cloud Experiment. I: single-layer cloud. *Q. J. R. Meteorol. Soc.*, **135**, 979–1002, 10.1002/qj.416.

Köhler, M., 2020: Cloud cover. *Chapter 3.8.5 in ICON Tutorial: Working with the ICON Model*, F. Prill, D. Reinert, D. Rieger, and G. Zängl, November 2020, 10.5676/dwd_pub/nwv/icon_tutorial2020.

794
795 Koo, M.-S., and S.-Y. Hong, 2010: Diurnal variations of simulated precipitation over East Asia
796 in two regional climate models. *J. Geophys. Res. Atmos.*, **115**, 10.1029/2009JD012574.
797 Koo, M.-S., S. Baek, K.-H. Seol, and K. Cho, 2017: Advances in land modeling of KIAPS based
798 on the Noah Land Surface Model. *Asia. Pac. J. Atmos. Sci.*, **53**, 361-373, 10.1007/s13143-017-
799 0043-2.
800 Kuo, Y.-H., K. A. Schiro, and J. D. Neelin, 2018: Convective Transition Statistics over Tropical
801 Oceans for Climate Model Diagnostics: Observational Baseline. *J. Atmos. Sci.*, **75**, 1553-1570,
802 10.1175/jas-d-17-0287.1.
803 Kuo, Y.-H., and Coauthors, 2020: Convective Transition Statistics over Tropical Oceans for
804 Climate Model Diagnostics: GCM Evaluation. *J. Atmos. Sci.*, **77**, 379-403, 10.1175/jas-d-19-
805 0132.1.
806 Larson, V. E., and J.-C. Golaz, 2005: Using Probability Density Functions to Derive Consistent
807 Closure Relationships among Higher-Order Moments. *Mon. Weather Rev.*, **133**, 1023-1042,
808 10.1175/mwr2902.1.
809 Larson, V. E., and D. P. Schanen, 2013: The Subgrid Importance Latin Hypercube Sampler
810 (SILHS): a multivariate subcolumn generator. *Geosci. Model Dev.*, **6**, 1813-1829, 10.5194/gmd-
811 6-1813-2013.
812 Larson, V. E., 2017: CLUBB-SILHS: A parameterization of subgrid variability in the
813 atmosphere, ArXiv:1711.03675 [Physics].
814 Lawrence, D. M., and Coauthors, 2019: The Community Land Model Version 5: Description of
815 New Features, Benchmarking, and Impact of Forcing Uncertainty. *J. Adv. Model. Earth Syst.*, **11**,
816 4245-4287, 10.1029/2018MS001583.
817 Lee, E.-H., E. Lee, R. Park, Y. C. Kwon, and S.-Y. Hong, 2018: Impact of Turbulent Mixing in
818 the Stratocumulus-Topped Boundary Layer on Numerical Weather Prediction. *Asia. Pac. J.*
819 *Atmos. Sci.*, **54**, 371-384, 10.1007/s13143-018-0024-0.
820 Lee, M.-I., S. D. Schubert, M. J. Suarez, J.-K. E. Schemm, H.-L. Pan, J. Han, and S.-H. Yoo,
821 2008: Role of convection triggers in the simulation of the diurnal cycle of precipitation over the
822 United States Great Plains in a general circulation model. *J. Geophys. Res. Atmos.*, **113**,
823 10.1029/2007JD008984.
824 Lee, W. L., and Coauthors, 2020: Taiwan Earth System Model Version 1: Description and
825 Evaluation of Mean State. *Geosci. Model Dev. Discuss.*, **2020**, 1-43, 10.5194/gmd-2019-377.
826 Lenderink, G., and Coauthors, 2004: The diurnal cycle of shallow cumulus clouds over land: A
827 single-column model intercomparison study. *Q. J. R. Meteorol. Soc.*, **130**, 3339-3364,
828 10.1256/qj.03.122.
829 Lin, W., and S. Xie, 2021: Frameworks for Testing and Evaluating Fast Physics
830 Parameterizations in Climate and Weather Forecasting Models. *Fast Physics in Large Scale*
831 *Atmospheric Models: Parameterization, Evaluation, and Observations*, Y. Liu, P. Kollias, and L.
832 J. Donner, Eds., in publish.
833 Ma, H.-Y., K. Zhang, S. Tang, S. Xie, and R. Fu, 2021a: Evaluation of the Causes of Wet-
834 Season Dry Biases Over Amazonia in CAM5. *J. Geophys. Res. Atmos.*, **126**, e2020JD033859,
835 10.1029/2020JD033859.
836 Ma, H. Y., and Coauthors, 2021b: A multi-year short-range hindcast experiment with CESM1
837 for evaluating climate model moist processes from diurnal to interannual timescales. *Geosci.*
838 *Model Dev.*, **14**, 73-90, 10.5194/gmd-14-73-2021.

Malardel, S., and P. Bechtold, 2019: The coupling of deep convection with the resolved flow via the divergence of mass flux in the IFS. *Q. J. R. Meteorol. Soc.*, **145**, 1832-1845, 10.1002/qj.3528.

Mapes, B., and R. Neale, 2011: Parameterizing Convective Organization to Escape the Entrainment Dilemma. *J. Adv. Model. Earth Syst.*, **3**, 10.1029/2011MS000042.

Martin, S. T., and Coauthors, 2016: Introduction: Observations and Modeling of the Green Ocean Amazon (GoAmazon2014/5). *Atmos. Chem. Phys.*, **16**, 4785-4797, 10.5194/acp-16-4785-2016.

McTaggart-Cowan, R., and Coauthors, 2019a: Modernization of Atmospheric Physics Parameterization in Canadian NWP. *J. Adv. Model. Earth Syst.*, **n/a**, 10.1029/2019ms001781.

McTaggart-Cowan, R., P. A. Vaillancourt, A. Zadra, L. Separovic, S. Corvec, and D. Kirshbaum, 2019b: A Lagrangian Perspective on Parameterizing Deep Convection. *Mon. Weather Rev.*, **147**, 4127-4149, 10.1175/mwr-d-19-0164.1.

McTaggart-Cowan, R., P. A. Vaillancourt, L. Separovic, S. Corvec, and A. Zadra, 2020: A Convection Parameterization for Low-CAPE Environments. *Mon. Weather Rev.*, **148**, 4917-4941, 10.1175/mwr-d-20-0020.1.

Morrison, H., and A. Gettelman, 2008: A New Two-Moment Bulk Stratiform Cloud Microphysics Scheme in the Community Atmosphere Model, Version 3 (CAM3). Part I: Description and Numerical Tests. *J. Climate*, **21**, 3642-3659, 10.1175/2008JCLI2105.1.

Morrison, H., and Coauthors, 2009: Intercomparison of model simulations of mixed-phase clouds observed during the ARM Mixed-Phase Arctic Cloud Experiment. II: Multilayer cloud. *Q. J. R. Meteorol. Soc.*, **135**, 1003-1019, 10.1002/qj.415.

Neale, R. B., and Coauthors, 2012: Description of the NCAR Community Atmosphere Model (CAM 5.0). NCAR Technical Note NCARTN-4861STR, 274 pp.

Neelin, J. D., O. Peters, and K. Hales, 2009: The Transition to Strong Convection. *J. Atmos. Sci.*, **66**, 2367-2384, 10.1175/2009jas2962.1.

Neggers, R. A. J., A. P. Siebesma, and T. Heus, 2012: Continuous Single-Column Model Evaluation at a Permanent Meteorological Supersite. *Bull. Amer. Meteor. Soc.*, **93**, 1389-1400, 10.1175/bams-d-11-00162.1.

Neggers, R. A. J., and A. P. Siebesma, 2013: Constraining a System of Interacting Parameterizations through Multiple-Parameter Evaluation: Tracing a Compensating Error between Cloud Vertical Structure and Cloud Overlap. *J. Climate*, **26**, 6698-6715, 10.1175/jcli-d-12-00779.1.

Neggers, R. A. J., 2015a: Exploring bin-macrophysics models for moist convective transport and clouds. *J. Adv. Model. Earth Syst.*, **7**, 2079-2104, 10.1002/2015ms000502.

———, 2015b: Attributing the behavior of low-level clouds in large-scale models to subgrid-scale parameterizations. *J. Adv. Model. Earth Syst.*, **7**, 2029-2043, 10.1002/2015MS000503.

Neggers, R. A. J., and Coauthors, 2017: Single-Column Model Simulations of Subtropical Marine Boundary-Layer Cloud Transitions Under Weakening Inversions. *J. Adv. Model. Earth Syst.*, **9**, 2385-2412, 10.1002/2017MS001064.

Oliveira, M. I., and Coauthors, 2020: Planetary boundary layer evolution over the Amazon rainforest in episodes of deep moist convection at the Amazon Tall Tower Observatory. *Atmos. Chem. Phys.*, **20**, 15-27, 10.5194/acp-20-15-2020.

Park, R.-S., J.-H. Chae, and S.-Y. Hong, 2016: A Revised Prognostic Cloud Fraction Scheme in a Global Forecasting System. *Mon. Weather Rev.*, **144**, 1219-1229, 10.1175/mwr-d-15-0273.1.

Park, S., and C. S. Bretherton, 2009: The University of Washington Shallow Convection and Moist Turbulence Schemes and Their Impact on Climate Simulations with the Community Atmosphere Model. *J. Climate*, **22**, 3449-3469, 10.1175/2008JCLI2557.1.

Park, S., 2014a: A Unified Convection Scheme (UNICON). Part I: Formulation. *J. Atmos. Sci.*, **71**, 3902-3930, 10.1175/jas-d-13-0233.1.

—, 2014b: A Unified Convection Scheme (UNICON). Part II: Simulation. *J. Atmos. Sci.*, **71**, 3931-3973, 10.1175/jas-d-13-0234.1.

Park, S., C. S. Bretherton, and P. J. Rasch, 2014: Integrating Cloud Processes in the Community Atmosphere Model, Version 5. *J. Climate*, **27**, 6821-6856, 10.1175/JCLI-D-14-00087.1.

Park, S., E.-H. Baek, B.-M. Kim, and S.-J. Kim, 2017: Impact of detrained cumulus on climate simulated by the Community Atmosphere Model Version 5 with a unified convection scheme. *J. Adv. Model. Earth Syst.*, **9**, 1399-1411, 10.1002/2016MS000877.

Park, S., J. Shin, S. Kim, E. Oh, and Y. Kim, 2019: Global Climate Simulated by the Seoul National University Atmosphere Model Version 0 with a Unified Convection Scheme (SAM0-UNICON). *J. Climate*, **32**, 2917-2949, 10.1175/jcli-d-18-0796.1.

Petch, J., and Coauthors, 2014: Evaluation of intercomparisons of four different types of model simulating TWP-ICE. *Q. J. R. Meteorol. Soc.*, **140**, 826-837, 10.1002/qj.2192.

Pithan, F., and Coauthors, 2016: Select strengths and biases of models in representing the Arctic winter boundary layer over sea ice: the Larcform 1 single column model intercomparison. *J. Adv. Model. Earth Syst.*, **8**, 1345-1357, 10.1002/2016MS000630.

Randall, D. A., K.-M. Xu, R. J. C. Somerville, and S. Iacobellis, 1996: Single-Column Models and Cloud Ensemble Models as Links between Observations and Climate Models. *J. Climate*, **9**, 1683-1697, 10.1175/1520-0442(1996)009<1683:SCMACE>2.0.CO;2.

Rasch, P. J., and Coauthors, 2019: An Overview of the Atmospheric Component of the Energy Exascale Earth System Model. *J. Adv. Model. Earth Syst.*, **11**, 2377-2411, 10.1029/2019ms001629.

Raschendorfer, M., 2000: The New Turbulence Parameterization in the Lokal-Modell of DWD. *Research Activities in Atmospheric and Oceanic Modelling*, WMO/TD-No.987, pg 4.30-4.31.

Rio, C., F. Hourdin, J. Y. Grandpeix, and J. P. Lafore, 2009: Shifting the diurnal cycle of parameterized deep convection over land. *Geophys. Res. Lett.*, **36**, 10.1029/2008GL036779.

Rio, C., and Coauthors, 2013: Control of deep convection by sub-cloud lifting processes: the ALP closure in the LMDZ5B general circulation model. *Clim Dyn.*, **40**, 2271-2292, 10.1007/s00382-012-1506-x.

Ruppert, J. H., and R. H. Johnson, 2015: Diurnally Modulated Cumulus Moistening in the Preonset Stage of the Madden-Julian Oscillation during DYNAMO. *J. Atmos. Sci.*, **72**, 1622-1647, 10.1175/JAS-D-14-0218.1.

Rutledge, S. A., and P. V. Hobbs, 1984: The Mesoscale and Microscale Structure and Organization of Clouds and Precipitation in Midlatitude Cyclones. XII: A Diagnostic Modeling Study of Precipitation Development in Narrow Cold-Frontal Rainbands. *J. Atmos. Sci.*, **41**, 2949-2972, 10.1175/1520-0469(1984)041<2949:Tmamsa>2.0.CO;2.

Schumacher, C., R. A. Houze, and I. Kraucunas, 2004: The Tropical Dynamical Response to Latent Heating Estimates Derived from the TRMM Precipitation Radar. *J. Atmos. Sci.*, **61**, 1341-1358, 10.1175/1520-0469(2004)061<1341:TTDRTL>2.0.CO;2.

Seifert, A., 2008: A Revised Cloud Microphysical Parameterization for COSMO-LME. *COSMO Newsl.*, 25-28.

Shin, H. H., and S.-Y. Hong, 2015: Representation of the Subgrid-Scale Turbulent Transport in Convective Boundary Layers at Gray-Zone Resolutions. *Mon. Weather Rev.*, **143**, 250-271, 10.1175/mwr-d-14-00116.1.

Shiu, C. J., and Coauthors, 2021: GTS v1.0: a macrophysics scheme for climate models based on a probability density function. *Geosci. Model Dev.*, **14**, 177-204, 10.5194/gmd-14-177-2021.

Stephens, G. L., and Coauthors, 2010: Dreary state of precipitation in global models. *J. Geophys. Res. Atmos.*, **115**, 10.1029/2010JD014532.

Stratton, R. A., and A. J. Stirling, 2012: Improving the diurnal cycle of convection in GCMs. *Q. J. R. Meteorol. Soc.*, **138**, 1121-1134, 10.1002/qj.991.

Sun, Y., S. Solomon, A. Dai, and R. W. Portmann, 2007: How Often Will It Rain? *J. Climate*, **20**, 4801-4818, 10.1175/jcli4263.1.

Sundqvist, H., E. Berge, and J. E. Kristjánsson, 1989: Condensation and Cloud Parameterization Studies with a Mesoscale Numerical Weather Prediction Model. *Mon. Weather Rev.*, **117**, 1641-1657, 10.1175/1520-0493(1989)117<1641:Cacpsw>2.0.Co;2.

Tang, S., and Coauthors, 2016: Large-scale vertical velocity, diabatic heating and drying profiles associated with seasonal and diurnal variations of convective systems observed in the GoAmazon2014/5 experiment. *Atmos. Chem. Phys.*, **16**, 14249-14264, 10.5194/acp-16-14249-2016.

Tang, S., and Coauthors, 2019: Differences in Eddy-Correlation and Energy-Balance Surface Turbulent Heat Flux Measurements and Their Impacts on the Large-Scale Forcing Fields at the ARM SGP Site. *J. Geophys. Res. Atmos.*, **124**, 3301-3318, 10.1029/2018jd029689.

Tang, S., P. Gleckler, S. Xie, J. Lee, M.-S. Ahn, C. Covey, and C. Zhang, 2021: Evaluating the Diurnal and Semidiurnal Cycle of Precipitation in CMIP6 Models Using Satellite- and Ground-Based Observations. *J. Climate*, **34**, 3189-3210, 10.1175/jcli-d-20-0639.1.

Taylor, K. E., R. J. Stouffer, and G. A. Meehl, 2012: An Overview of CMIP5 and the Experiment Design. *Bull. Amer. Meteor. Soc.*, **93**, 485-498, 10.1175/bams-d-11-00094.1.

Thayer-Calder, K., and Coauthors, 2015: A unified parameterization of clouds and turbulence using CLUBB and subcolumns in the Community Atmosphere Model. *Geosci. Model Dev.*, **8**, 3801-3821, 10.5194/gmd-8-3801-2015.

Tian, Y., Y. Zhang, S. A. Klein, and C. Schumacher, 2021: Interpreting the Diurnal Cycle of Clouds and Precipitation in the ARM GoAmazon Observations: Shallow to Deep Convection Transition. *J. Geophys. Res. Atmos.*, **126**, e2020JD033766, 10.1029/2020JD033766.

Trenberth, K. E., A. Dai, R. M. Rasmussen, and D. B. Parsons, 2003: The Changing Character of Precipitation. *Bull. Amer. Meteor. Soc.*, **84**, 1205-1218, 10.1175/bams-84-9-1205.

Varble, A. C., and Coauthors, 2021: Utilizing a Storm-Generating Hotspot to Study Convective Cloud Transitions: The CACTI Experiment. *Bull. Amer. Meteor. Soc.*, **102**, E1597-E1620, 10.1175/bams-d-20-0030.1.

Wang, Y.-C., and H.-H. Hsu, 2019: Improving diurnal rainfall phase over the Southern Great Plains in warm seasons by using a convective triggering design. *Int. J. Climatol.*, **39**, 5181-5190, 10.1002/joc.6117.

Wang, Y.-C., S. Xie, S. Tang, and W. Lin, 2020: Evaluation of an Improved Convective Triggering Function: Observational Evidence and SCM Tests. *J. Geophys. Res. Atmos.*, **125**, e2019JD031651, 10.1029/2019jd031651.

Wang, Y., L. Zhou, and K. Hamilton, 2007: Effect of Convective Entrainment/Detrainment on the Simulation of the Tropical Precipitation Diurnal Cycle. *Mon. Weather Rev.*, **135**, 567-585, 10.1175/mwr3308.1.

975 Wang, Y. C., H. L. Pan, and H. H. Hsu, 2015: Impacts of the triggering function of cumulus
 976 parameterization on warm-season diurnal rainfall cycles at the Atmospheric Radiation
 977 Measurement Southern Great Plains site. *J. Geophys. Res. Atmos.*, **120**, 10,681-10,702,
 978 10.1002/2015JD023337.
 979 Wei, Y., Z. Pu, and C. Zhang, 2020: Diurnal Cycle of Precipitation Over the Maritime Continent
 980 Under Modulation of MJO: Perspectives From Cloud-Permitting Scale Simulations. *J. Geophys.*
 981 *Res. Atmos.*, **125**, e2020JD032529, 10.1029/2020JD032529.
 982 Wyant, M. C., and Coauthors, 2007: A single-column model intercomparison of a heavily
 983 drizzling stratocumulus-topped boundary layer. *J. Geophys. Res. Atmos.*, **112**,
 984 10.1029/2007jd008536.
 985 Xie, S., and M. Zhang, 2000: Impact of the convection triggering function on single-column
 986 model simulations. *J. Geophys. Res. Atmos.*, **105**, 14983-14996, 10.1029/2000JD900170.
 987 Xie, S., and Coauthors, 2002: Intercomparison and evaluation of cumulus parametrizations under
 988 summertime midlatitude continental conditions. *Q. J. R. Meteorol. Soc.*, **128**, 1095-1135,
 989 10.1256/003590002320373229.
 990 Xie, S., R. T. Cederwall, and M. Zhang, 2004: Developing long-term single-column model/cloud
 991 system-resolving model forcing data using numerical weather prediction products constrained by
 992 surface and top of the atmosphere observations. *J. Geophys. Res. Atmos.*, **109**,
 993 10.1029/2003jd004045.
 994 Xie, S., and Coauthors, 2005: Simulations of midlatitude frontal clouds by single-column and
 995 cloud-resolving models during the Atmospheric Radiation Measurement March 2000 cloud
 996 intensive operational period. *J. Geophys. Res. Atmos.*, **110**, D15S03, 10.1029/2004JD005119.
 997 Xie, S., and Coauthors, 2018: Understanding Cloud and Convective Characteristics in Version 1
 998 of the E3SM Atmosphere Model. *J. Adv. Model. Earth Syst.*, **10**, 2618-2644,
 999 10.1029/2018MS001350.
 1000 Xie, S., and Coauthors, 2019: Improved Diurnal Cycle of Precipitation in E3SM With a Revised
 1001 Convective Triggering Function. *J. Adv. Model. Earth Syst.*, **11**, 2290-2310,
 1002 10.1029/2019ms001702.
 1003 Xu, K.-M., and Coauthors, 2005: Modeling springtime shallow frontal clouds with cloud-
 1004 resolving and single-column models. *J. Geophys. Res. Atmos.*, **110**, 10.1029/2004JD005153.
 1005 Yanai, M., S. Esbensen, and J.-H. Chu, 1973: Determination of Bulk Properties of Tropical
 1006 Cloud Clusters from Large-Scale Heat and Moisture Budgets. *J. Atmos. Sci.*, **30**, 611-627,
 1007 10.1175/1520-0469(1973)030<0611:DOBPOT>2.0.CO;2.
 1008 Zängl, G., D. Reinert, P. Rípodas, and M. Baldauf, 2015: The ICON (ICOsahedral Non-
 1009 hydrostatic) modelling framework of DWD and MPI-M: Description of the non-hydrostatic
 1010 dynamical core. *Q. J. R. Meteorol. Soc.*, **141**, 563-579, 10.1002/qj.2378.
 1011 Zermeno-Díaz, D. M., C. Zhang, P. Kollias, and H. Kalesse, 2015: The Role of Shallow Cloud
 1012 Moistening in MJO and Non-MJO Convective Events over the ARM Manus Site. *J. Atmos. Sci.*,
 1013 **72**, 4797-4820, 10.1175/JAS-D-14-0322.1.
 1014 Zhang, G. J., and N. A. McFarlane, 1995: Sensitivity of climate simulations to the
 1015 parameterization of cumulus convection in the Canadian climate centre general circulation
 1016 model. *Atmosphere-Ocean*, **33**, 407-446, 10.1080/07055900.1995.9649539.
 1017 Zhang, G. J., 2003: Roles of tropospheric and boundary layer forcing in the diurnal cycle of
 1018 convection in the U.S. southern great plains. *Geophys. Res. Lett.*, **30**, 10.1029/2003GL018554.
 1019 Zhang, M., and J. Lin, 1997: Constrained Variational Analysis of Sounding Data Based on
 1020 Column-Integrated Budgets of Mass, Heat, Moisture, and Momentum: Approach and

1021 Application to ARM Measurements. *J. Atmos. Sci.*, **54**, 1503-1524, 10.1175/1520-
1022 0469(1997)054<1503:CVAOSD>2.0.CO;2.
1023 Zhang, M., J. Lin, R. T. Cederwall, J. J. Yio, and S. C. Xie, 2001: Objective Analysis of ARM
1024 IOP Data: Method and Sensitivity. *Mon. Weather Rev.*, **129**, 295-311, 10.1175/1520-
1025 0493(2001)129<0295:OAOAID>2.0.CO;2.
1026 Zhang, M., R. C. J. Somerville, and S. Xie, 2016: The SCM Concept and Creation of ARM
1027 Forcing Datasets. *Meteorological Monographs*, **57**, 24.1-24.12, 10.1175/AMSMONOGRAPHS-
1028 D-15-0040.1.
1029 Zhang, Y., and S. A. Klein, 2010: Mechanisms Affecting the Transition from Shallow to Deep
1030 Convection over Land: Inferences from Observations of the Diurnal Cycle Collected at the ARM
1031 Southern Great Plains Site. *J. Atmos. Sci.*, **67**, 2943-2959, 10.1175/2010JAS3366.1.
1032 Zhu, P., and Coauthors, 2005: Intercomparison and Interpretation of Single-Column Model
1033 Simulations of a Nocturnal Stratocumulus-Topped Marine Boundary Layer. *Mon. Weather Rev.*,
1034 **133**, 2741-2758, 10.1175/mwr2997.1.
1035

1036 Table Captions:

1037 Table 1: Participating models and their basic information

1038 Table 2: Deep convective parameterizations in the participating SCMs

1039 Table 3: Model information for sensitivity study.

1040

1041 Figure Captions:

1042 Figure 1: Diurnal cycle of total precipitation averaged for the selected afternoon and nocturnal
1043 precipitation days during the MC3E field campaign.

1044 Figure 2: (Top) the composite diurnal cycle timeseries and (bottom) the harmonic dial plots of
1045 total precipitation averaged for the long-term simulation periods at (left) SGP and (right) MAO.
1046 The gray shading in the timeseries indicates $1.96\times$ standard error (95% confidence) of the
1047 observed precipitation. The radius and phase of the harmonic dial plots represent the amplitude
1048 (mm/day) and the peak hour (LST), respectively, of the first Fourier component of DCP.

1049 Figure 3: As in Figure 2 but for (left) wet season (December – March) and (right) dry season
1050 (July – October) at MAO.

1051 Figure 4: Diurnal cycle of cloud fraction from observations and simulations at (left) SGP and
1052 (right) MAO.

1053 Figure 5: The relationship between precipitation and CRH for (left) SGP and (right) MAO: (top)
1054 the precipitation amount averaged for each CRH bin; (middle) the probability of precipitation
1055 exceeding 1 mm/day for each CRH bin; (bottom) the occurrence frequency of each CRH bin.
1056 CRH is binned in intervals of 2%.

1057 Figure 6: Diurnal cycle timeseries of (top) total precipitation rate, (middle) convective
1058 precipitation fraction, and (bottom) harmonic dial plots of total precipitation averaged for the
1059 selected afternoon precipitation days during the long-term simulation periods at (left) SGP and
1060 (right) MAO.

1061 Figure 7: Percentage of days that the diurnal maximum precipitation occurs at each hour. The
1062 total number of cases are 136 days for SGP and 111 days for MAO.

1063 Figure 8: (Top) apparent heating (Q_1) and (bottom) drying (Q_2) averaged between 12 and 20 LST
1064 for selected afternoon precipitation days during the long-term simulation periods at (left) SGP
1065 and (right) MAO.

1066 Figure 9: The mean (dot, circle or diamond), median (cross), 25th and 75th percentiles (vertical
1067 lines) of precipitation onset time for the afternoon precipitation days at (left) SGP and (right)
1068 MAO. Models for sensitivity studies in Section 4 are also shown here in thin lines.

1069 Figure 10: As in Figure 6 but for selected nocturnal precipitation days.

1070 Figure 11: Precipitation rates from different components in CMC model for selected nocturnal
1071 precipitation days.

1072 Figure 12: Q_1 and Q_2 averaged between 00 and 06 LST for selected nocturnal precipitation days
1073 at (left) SGP and (right) MAO.

1074 Figure 13: As in Figure 6 but for selected models/configurations for sensitivity study. Sensitivity
1075 runs are indicated by dashed/dotted lines and open symbols. Note that the convective
1076 precipitation fraction for EAMv1.SILHS (blue dotted line) is zero because the convective and
1077 large-scale precipitation is unified in CLUBB-SILHS.

1078 Figure 14: As in Figure 13 but for nocturnal precipitation days.

1079 Figure 15: The diurnal cycle of (top) surface latent heat, (middle) sensible heat fluxes and
1080 (bottom) ground heat flux (net radiative fluxes minus latent and sensible heat fluxes) averaged
1081 for the long-term simulation periods at (left) SGP and (right) MAO. The diurnal cycle averaged
1082 in afternoon and nocturnal precipitation days have similar performance (not shown).

1083

1084 Table 1: Participating models and their basic information

Model name	Full name	Vertical levels	Timestep	turbulence	Stratiform clouds	Shallow convection	References	Contact Person
EAMv1	The E3SM* Atmospheric Model V1	72	30min	CLUBB	MG2, CLUBB	CLUBB	Rasch et al. (2019); Bogenschutz et al. (2020)	Shaocheng Xie, Shuaiqi Tang
EAMv1.trigger**	EAMv1 with revised convective trigger	72	30min	CLUBB	MG2, CLUBB	CLUBB	Xie et al. (2019)	Shaocheng Xie, Shuaiqi Tang
EAMv1.SILHS	EAMv1 with CLUBB-SILHS	72	30min	CLUBB	MG2, CLUBB-SILHS	CLUBB-SILHS	Guo et al. (2021)	Vincent Larson, Zhun Guo
SCAM6	Single Column Atmosphere Model Version 6	32	20min	CLUBB	MG2, CLUBB	CLUBB	Gottelman et al. (2019)	Shuaiqi Tang
SCAM5	Single Column Atmosphere Model Version 5	30	20min	UW-diag_TKE	MG, Park1	UW-PB09	Neale et al. (2012)	Shuaiqi Tang
SAM0-UNICON	Seoul National University Atmosphere Model	30	20min	UW-diag_TKE	MG, Park2	UNICON	Park et al. (2019)	Sungsu Park, Jihoon Shin
SKIM	Single Column Korean Integrated Model	64	10min	Shin-Hong	WSM5, PCH16	HanPan	Hong et al. (2013); Hong et al. (2018)	Myung-Seo Koo, Song-You Hong
CMC	Canadian Meteorological Center	84	450sec	TKE1.5	Sundqvist	M-Bechtold	McTaggart-Cowan et al. (2019a)	Paul Vaillancourt, Jing Yang
SMPCP	Stochastic MultiCloud Plume Convective Parameterization	30	20min	HB	MG, Park1	Unified Stochastic Plume-ZM	Khouider et al. (2021)	Boualem Khouider, Phani Murali Krishna
TaiESM1	Taiwan Earth System Model Version 1	30	30min	UW-diag_TKE	MG, GTS	UW-PB09	Lee et al. (2020)	Yi-Chi Wang
ICON	Icosahedral Nonhydrostatic Weather and Climate Model	90	2min	Raschendorf er00	Seifert08, Köhler20	Bechtold14	Zängl et al. (2015); Bařták Ďurán et al. (2021)	Martin Köhler, Daniel Klocke

*the full names and references of the acronyms and physical schemes are given in the Appendix.

**The results of EAMv1.trigger, EAMv1.SILHS and SCAM5 are only shown in the sensitivity studies in Section 4.

1085
1086
1087

1088 Table 2: Deep convective parameterizations in the participating SCMs

Model name	Deep convection	closure	Convective trigger	downdraft	reference
EAMv1	Zhang-McFarlane scheme (ZM)	Dilute CAPE	(1) CAPE >70 J/kg (2) The air parcel launch level is chosen within the boundary layer	Starts from updraft-top mass flux	Xie et al. (2018)
EAMv1.t rigger	ZM with revised convective trigger	Dilute CAPE	(1) CAPE >0 (2) dCAPE >0 (3) The air parcel launch level is chosen between the surface and 600 hPa	Same as EAMv1	Xie et al. (2019)
EAMv1.S ILHS	CLUBB-SILHS	No explicit closure	Not needed	Rain evaporation affect fluxes	Thayer-Calder et al. (2015); Griffin and Larson (2016)
SCAM6	ZM	Dilute CAPE	(1) CAPE >70 J/kg (2) The air parcel launch level is chosen within the boundary layer	Downdraft starts from updraft-top mass flux	Gettelman et al. (2019)
SCAM5	ZM	Dilute CAPE	Same as SCAM6	Same as SCAM6	Neale et al. (2012)
SAM0-UNICON	UNICON	No explicit closure	Not needed	Downdraft generated from updraft	Park (2014a, 2014b)
SKIM	KSAS	Quasi-equilibrium closure considering boundary-layer forcing	(1) $P_{\text{parcel_start}} - P_{\text{LFC}} < P_{\text{crit}}(\text{RH}_{\text{low}})$ (2) $P_{\text{LFC_w/o_ent}} - P_{\text{LFC_w/ent}} < 25 \text{ hPa}$ (3) $\text{CIN} < -120 \text{ m}^2 \text{ s}^{-2}$ (4) cloud depth > 150 hPa (5) cloud work function > 0	Starts from the level of minimum moist static energy between LFC and 450 hPa	Han et al. (2020)
CMC	Modified Kain-Fritsch (KF) with a mid-level elevated convective scheme	CAPE	(1) mixed parcel from PBL lifted to LCL to which a temperature perturbation is added is buoyant (2) cloud depth > 3000 m	Initiated at level of free sink	Kain and Fritsch (1990, 1992); McTaggart-Cowan et al. (2020)
SMCPCP	Unified Stochastic Plume-ZM	Weighted kinetic energy and CAPE	Same as SCAM6	Same as SCAM6	Khouider et al. (2021)
TaiESM1	ZM with revised convective trigger	Dilute CAPE	(1) CAPE >70 J/kg (2) $P_{\text{parcel_start}} - P_{\text{LFC}} < 150 \text{ hPa}$ (3) The air parcel launch level is chosen between the surface and 600 hPa	Same as SCAM6	Wang and Hsu (2019)
ICON	Bechtold14	CAPE	Entraining parcels starting with levels up to 350hPa above the surface that must detect cloud layer thicker than 200hPa.	Starts from Level of Free Sinking (LFS) $M(\text{LFS}) = -0.3M(\text{up,base})$	Bechtold et al. (2014)

1089

1090

1091 Table 3: Model information for sensitivity study.

Model name	Model features	Reference
EAMv1	Deep convection: ZM with convective trigger: (1) CAPE >70 J/kg (2) The air parcel launch level is chosen within the boundary layer	
EAMv1.trigger	Deep convection: ZM with convective trigger: (1) CAPE >0 (2) dCAPE >0 (3) The air parcel launch level is chosen between the surface and 600 hPa	Xie et al. (2019)
EAMv1.SILHS	Deep convection: CLUBB-SILHS	Thayer-Calder et al. (2015); Larson (2017)
SAM0-UNICON	Turbulence: diag_TKE Stratiform clouds: MG, Park1 Shallow Convection: UNICON Deep convection: UNICON	Park et al. (2019)
SCAM6	Turbulence: CLUBB Stratiform clouds: MG2, CLUBB Shallow Convection: CLUBB Deep convection: ZM	Gettelman et al. (2019)
SCAM5	Turbulence: diag_TKE Stratiform clouds: MG, Park1 Shallow Convection: PB09 Deep convection: ZM	Neal et al. (2012)
SCAM6.land	Interactive land	
SKIM.land	Interactive land	
SKIM.nudge	Nudging temperature and moisture	

1092

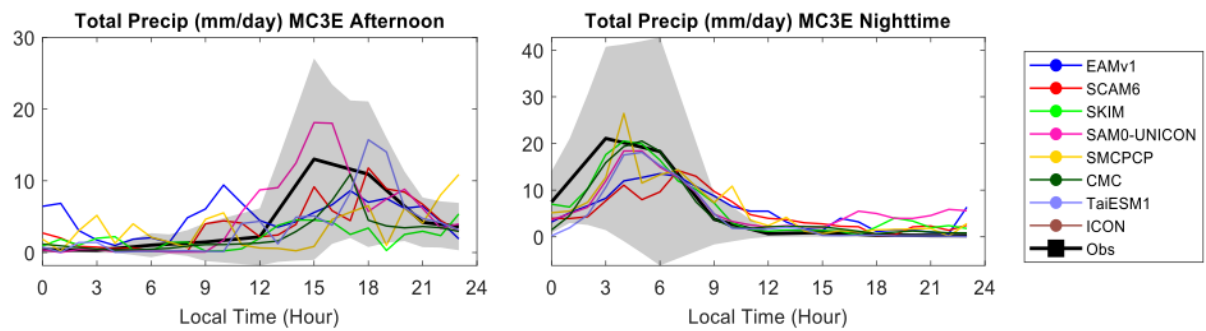
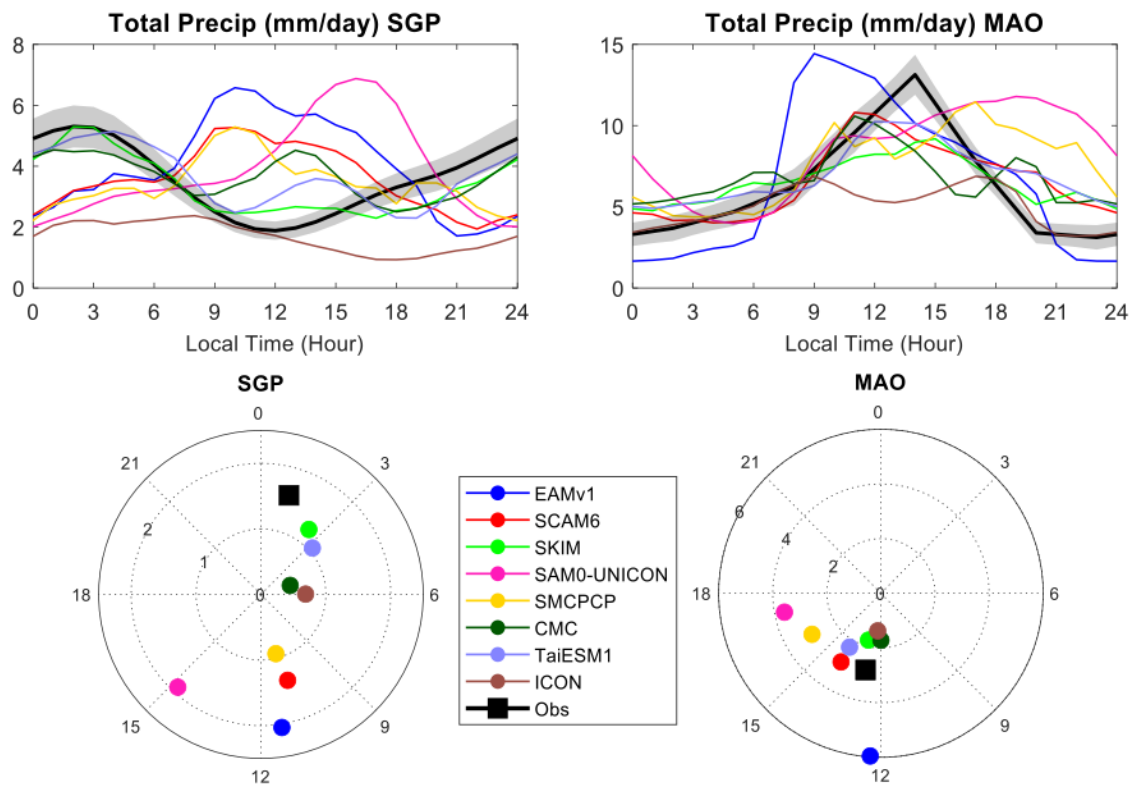


Figure 1: Diurnal cycle of total precipitation averaged for the selected afternoon and nocturnal precipitation days during the MC3E field campaign.

1102



1103

1104

1105

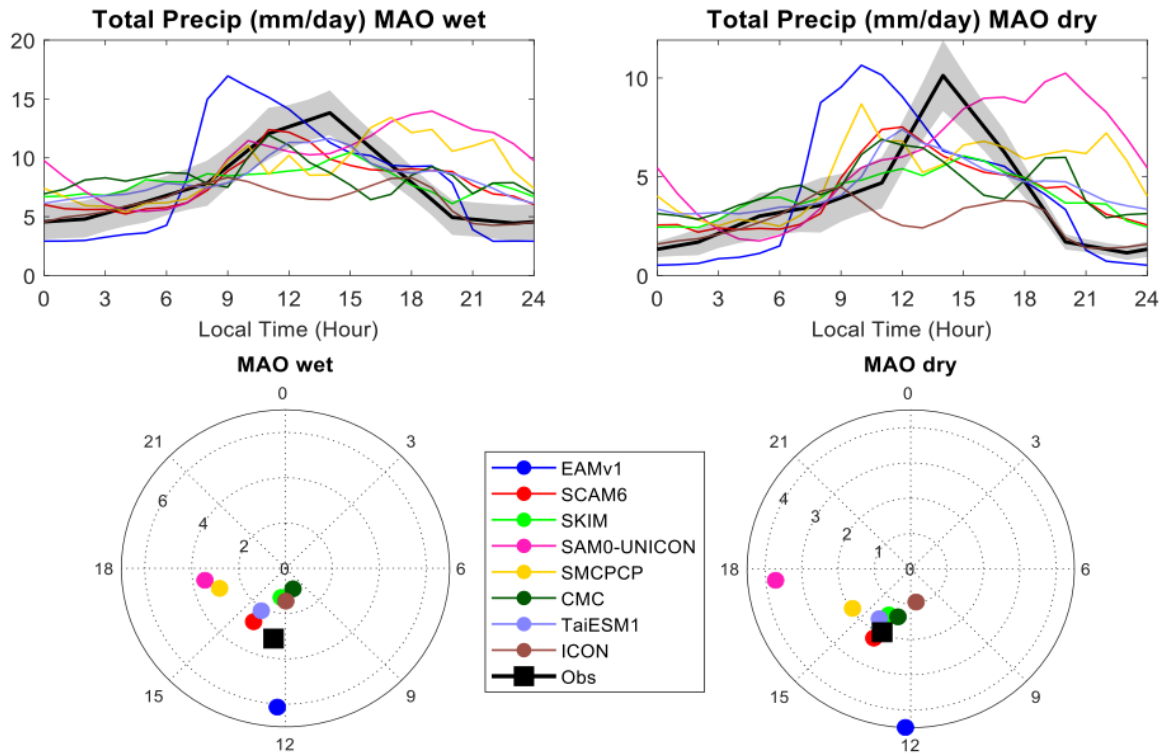
1106

1107

1108

1109

Figure 2: (Top) the composite diurnal cycle timeseries and (bottom) the harmonic dial plots of total precipitation averaged for the long-term simulation periods at (left) SGP and (right) MAO. The gray shading in the timeseries indicates $1.96\times$ standard error (95% confidence) of the observed precipitation. The radius and phase of the harmonic dial plots represent the amplitude (mm/day) and the peak hour (LST), respectively, of the first Fourier component of DCP.



1110

1111 Figure 3: As in Figure 2 but for (left) wet season (December – March) and (right) dry season
 1112 (July – October) at MAO.

1113

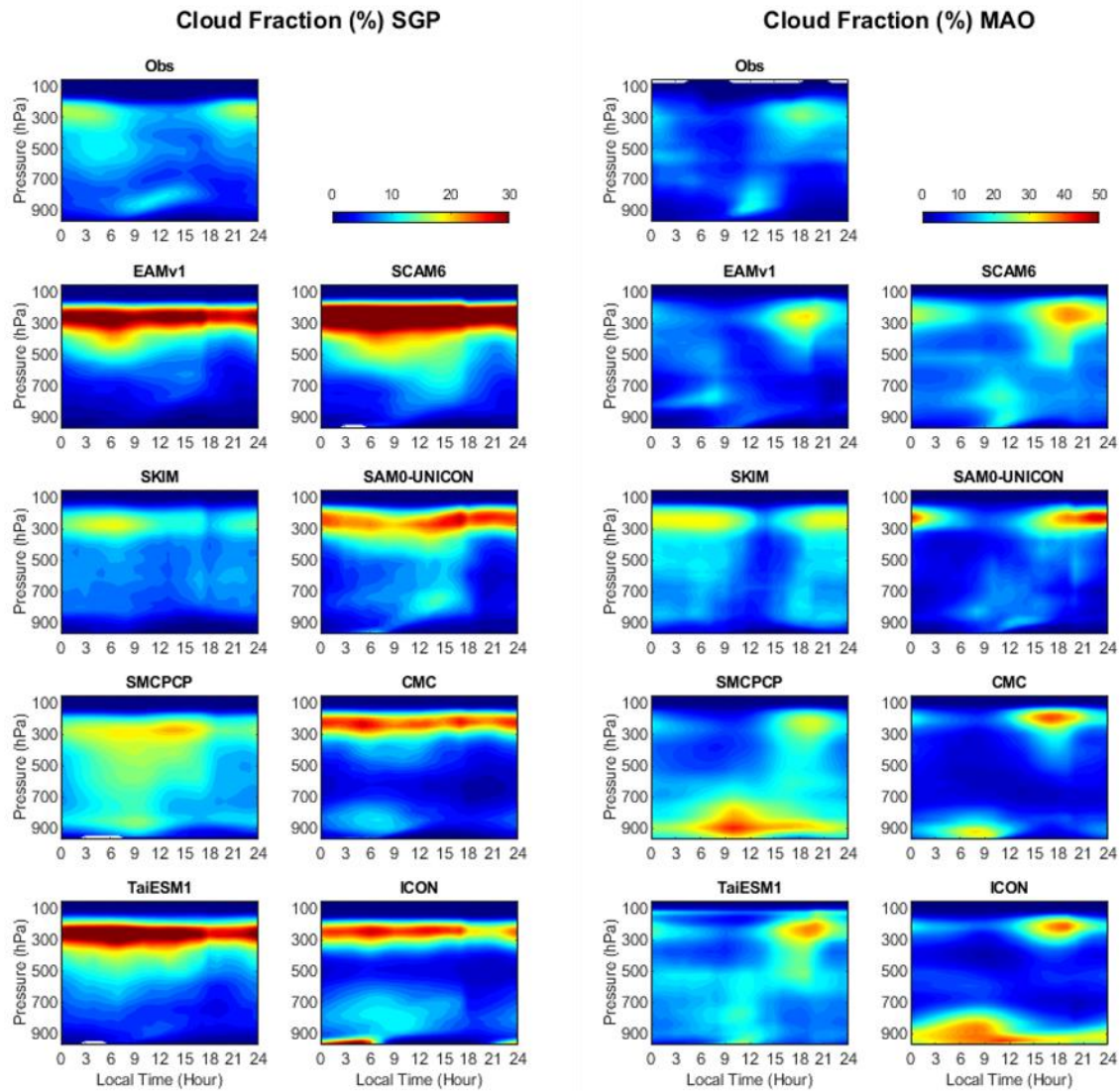


Figure 4: Diurnal cycle of cloud fraction from observations and simulations at (left) SGP and (right) MAO.

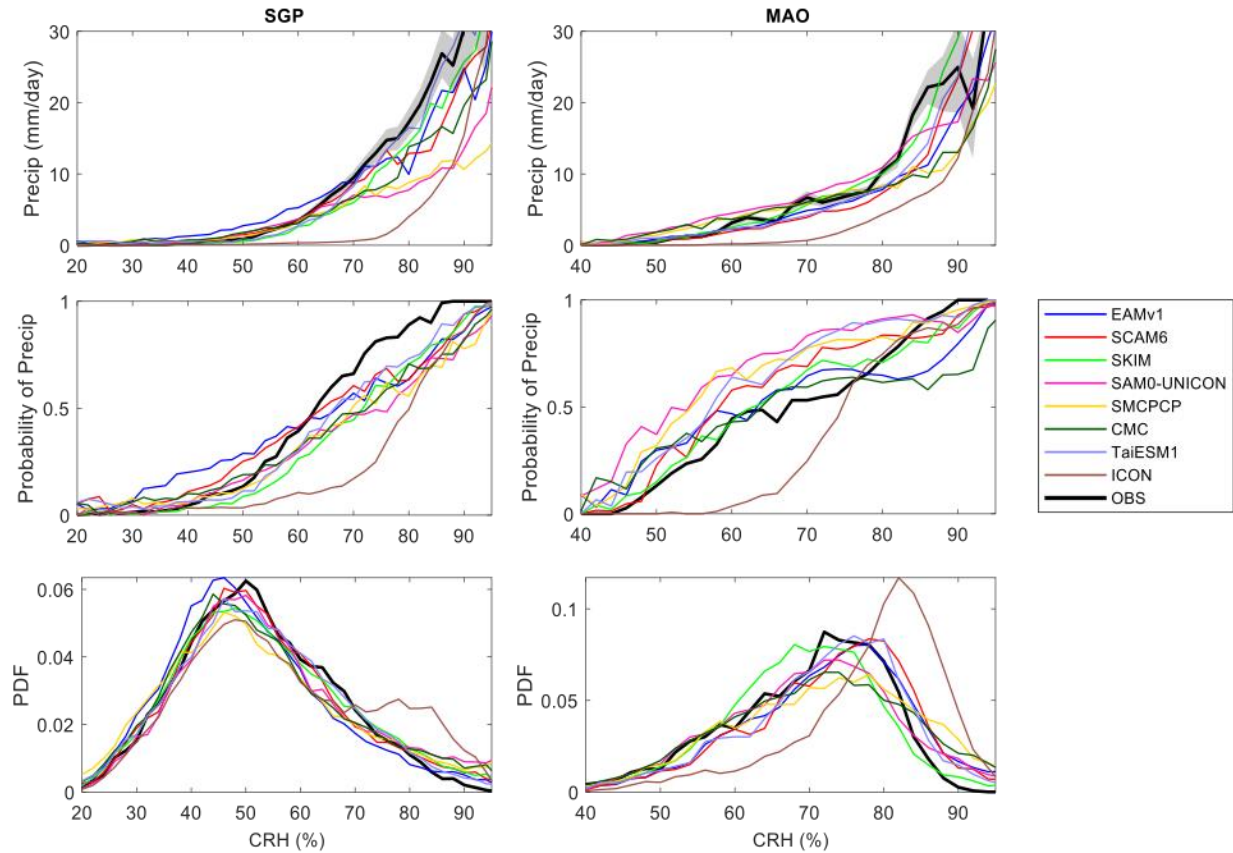


Figure 5: The relationship between precipitation and CRH for (left) SGP and (right) MAO: (top) the precipitation amount averaged for each CRH bin; (middle) the probability of precipitation exceeding 1 mm/day for each CRH bin; (bottom) the occurrence frequency of each CRH bin. CRH is binned in intervals of 2%.

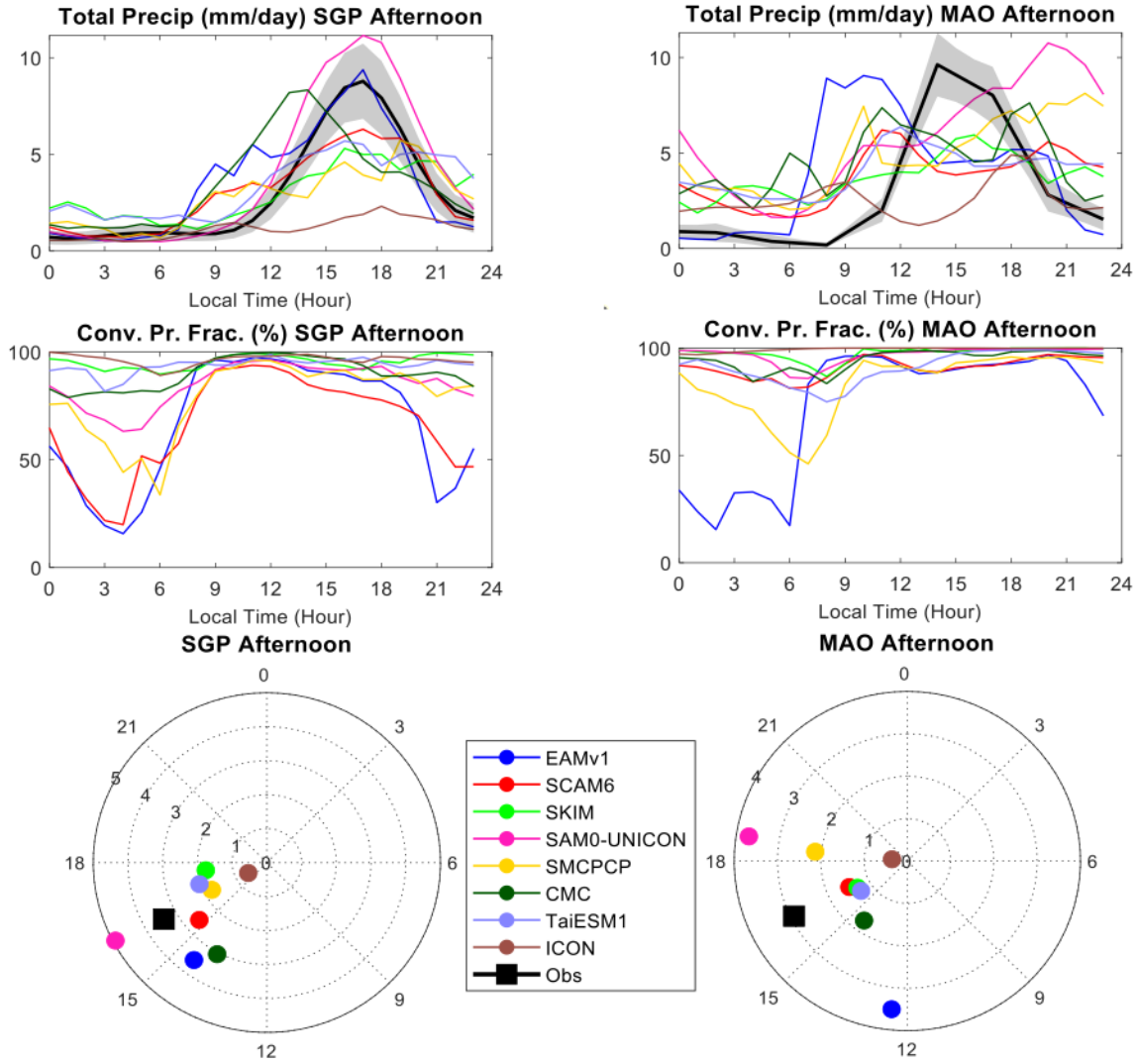
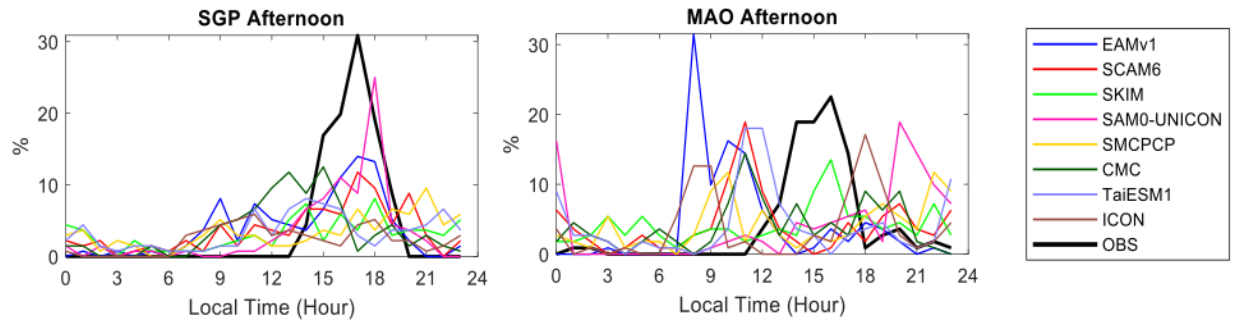


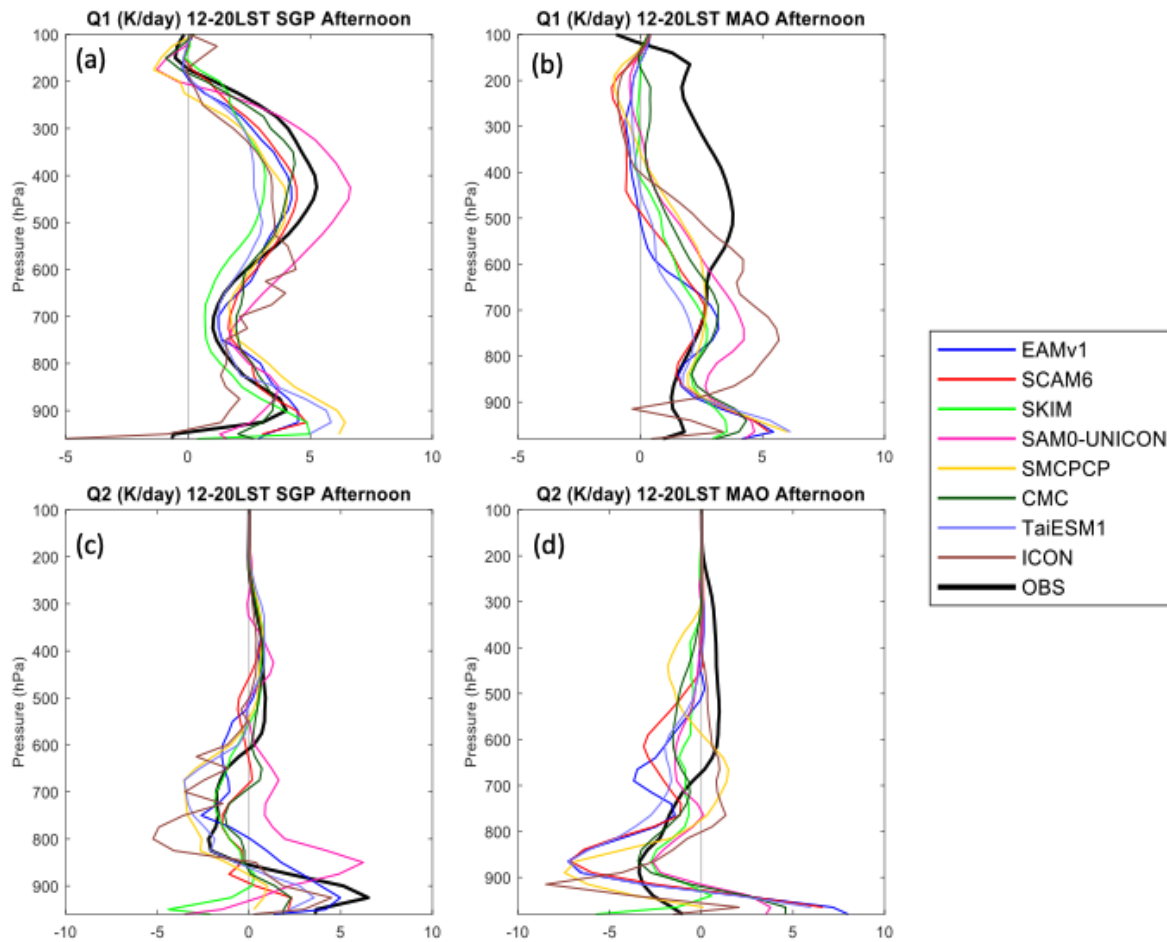
Figure 6: Diurnal cycle timeseries of (top) total precipitation rate, (middle) convective precipitation fraction, and (bottom) harmonic dial plots of total precipitation averaged for the selected afternoon precipitation days during the long-term simulation periods at (left) SGP and (right) MAO.



1130

1131 Figure 7: Percentage of days that the diurnal maximum precipitation occurs at each hour. The
 1132 total number of cases are 136 days for SGP and 111 days for MAO.

1133



1134 |

1135 Figure 8: (Top) apparent heating (Q_1) and (bottom) drying (Q_2) averaged between 12 and 20 LST

1136 for selected afternoon precipitation days during the long-term simulation periods at (left) SGP

1137 and (right) MAO.

1138

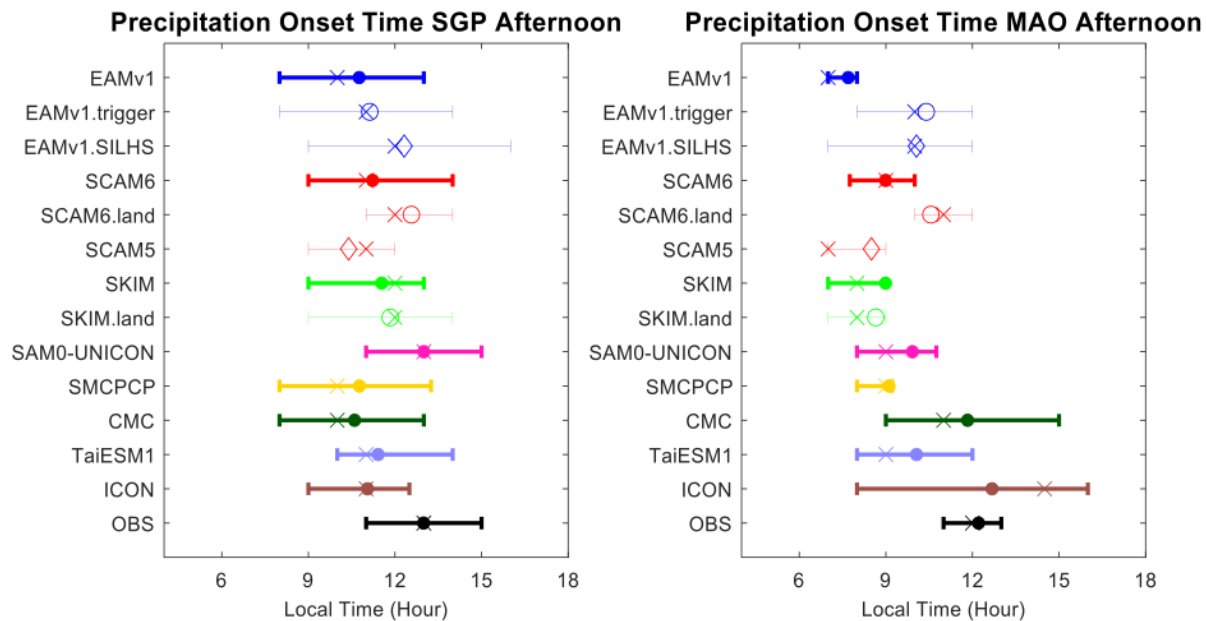
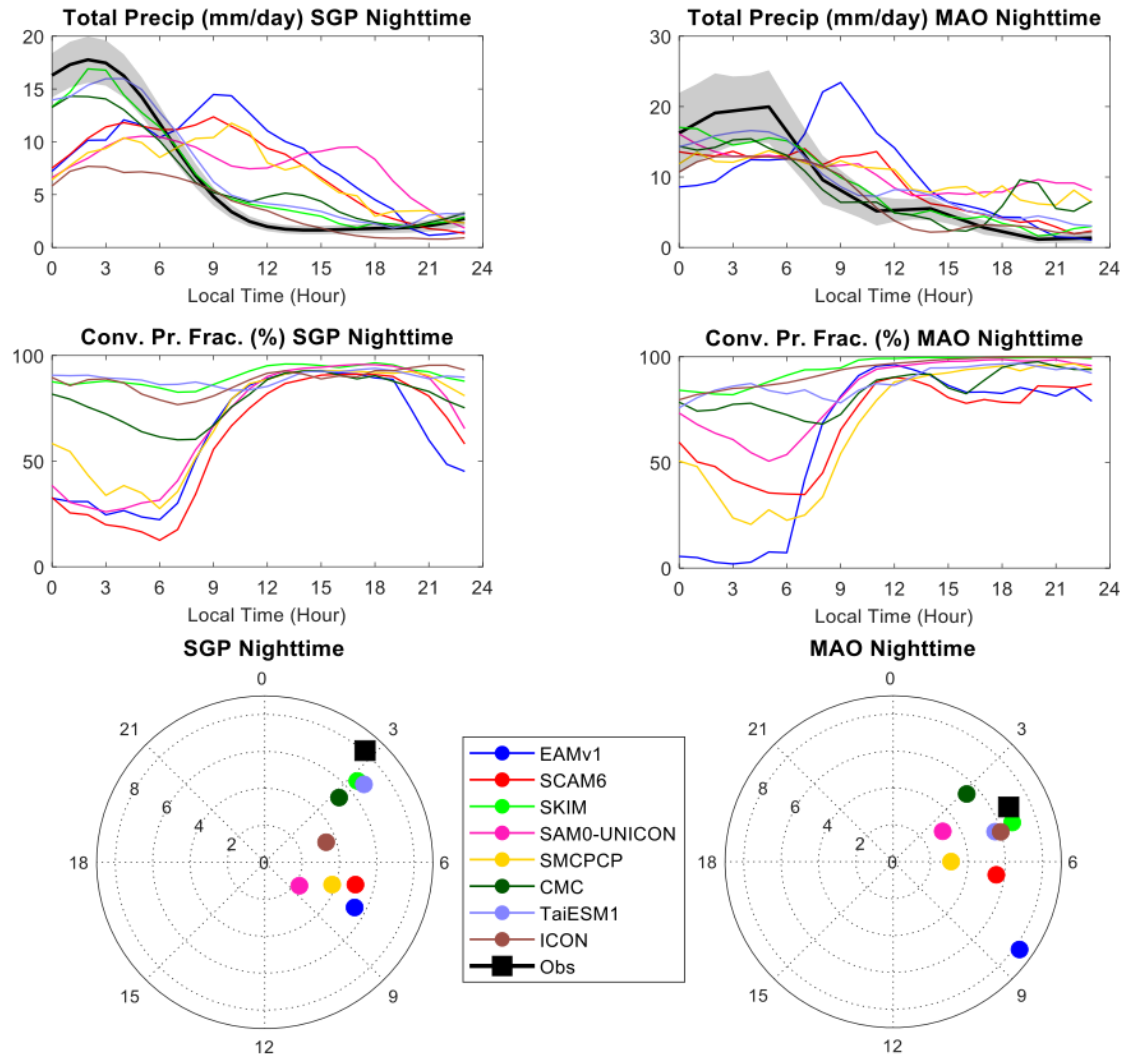


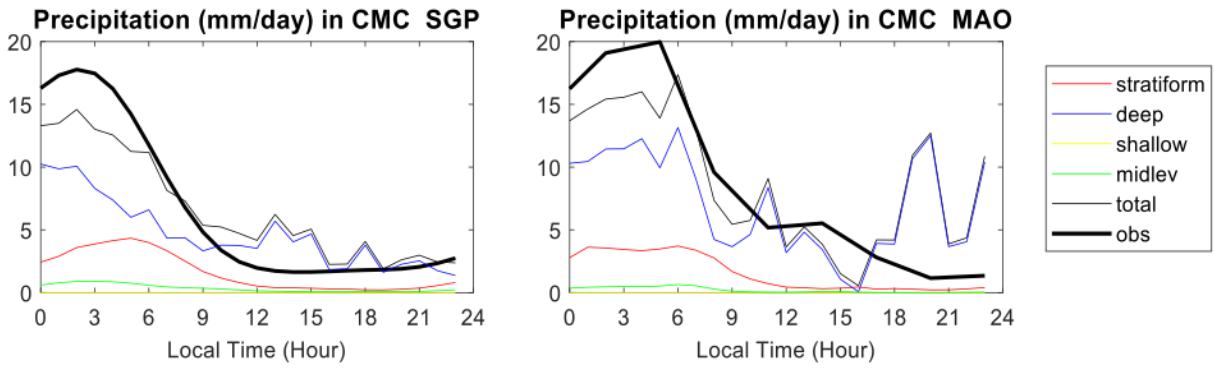
Figure 9: The mean (dot, circle or diamond), median (cross), 25th and 75th percentiles (vertical lines) of precipitation onset time for the afternoon precipitation days at (left) SGP and (right) MAO. Models for sensitivity studies in Section 4 are also shown here in thin lines.



1144

1145 Figure 10: As in Figure 6 but for selected nocturnal precipitation days.

1146



1147

1148

Figure 11: Precipitation rates from different components in CMC model for selected nocturnal precipitation days.

1149

1150

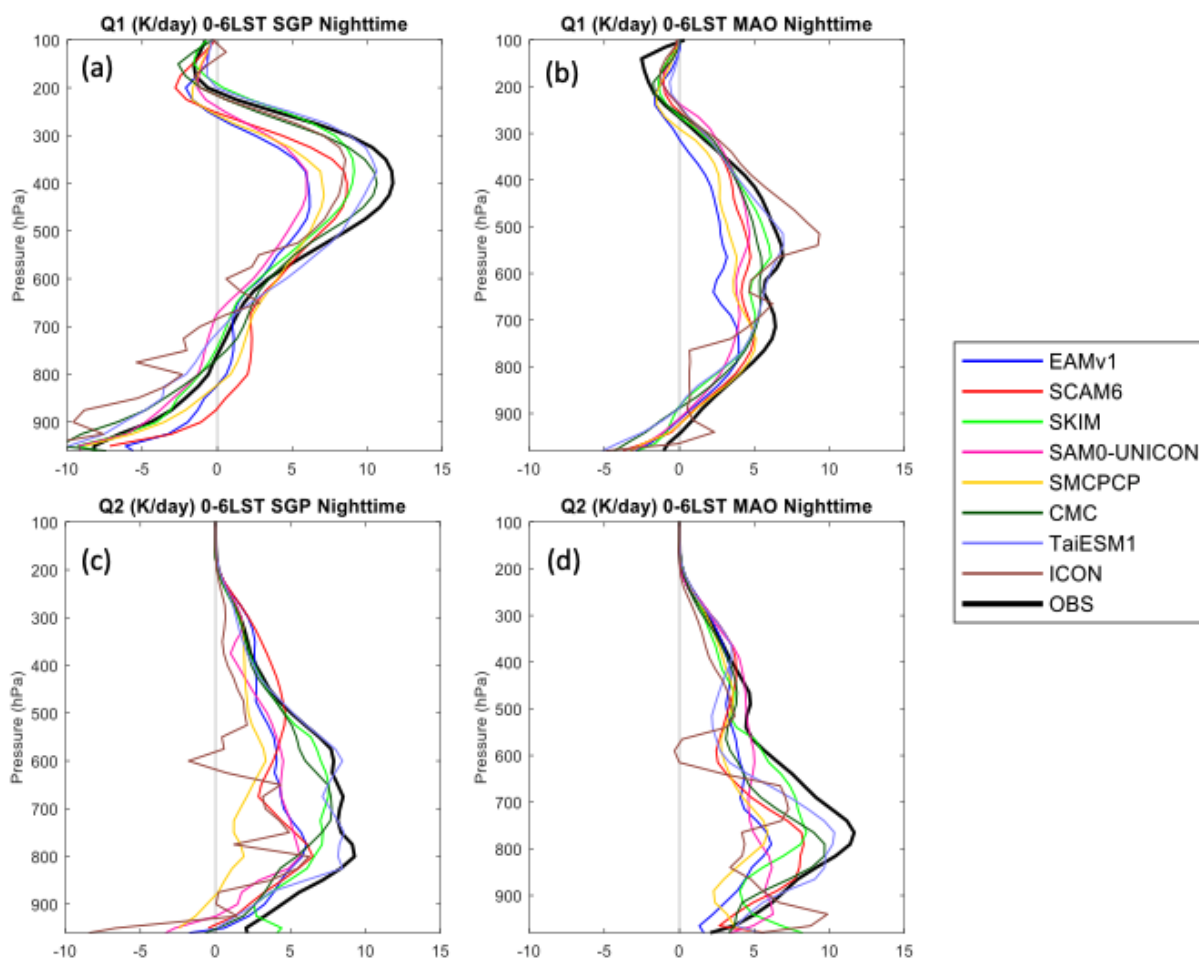
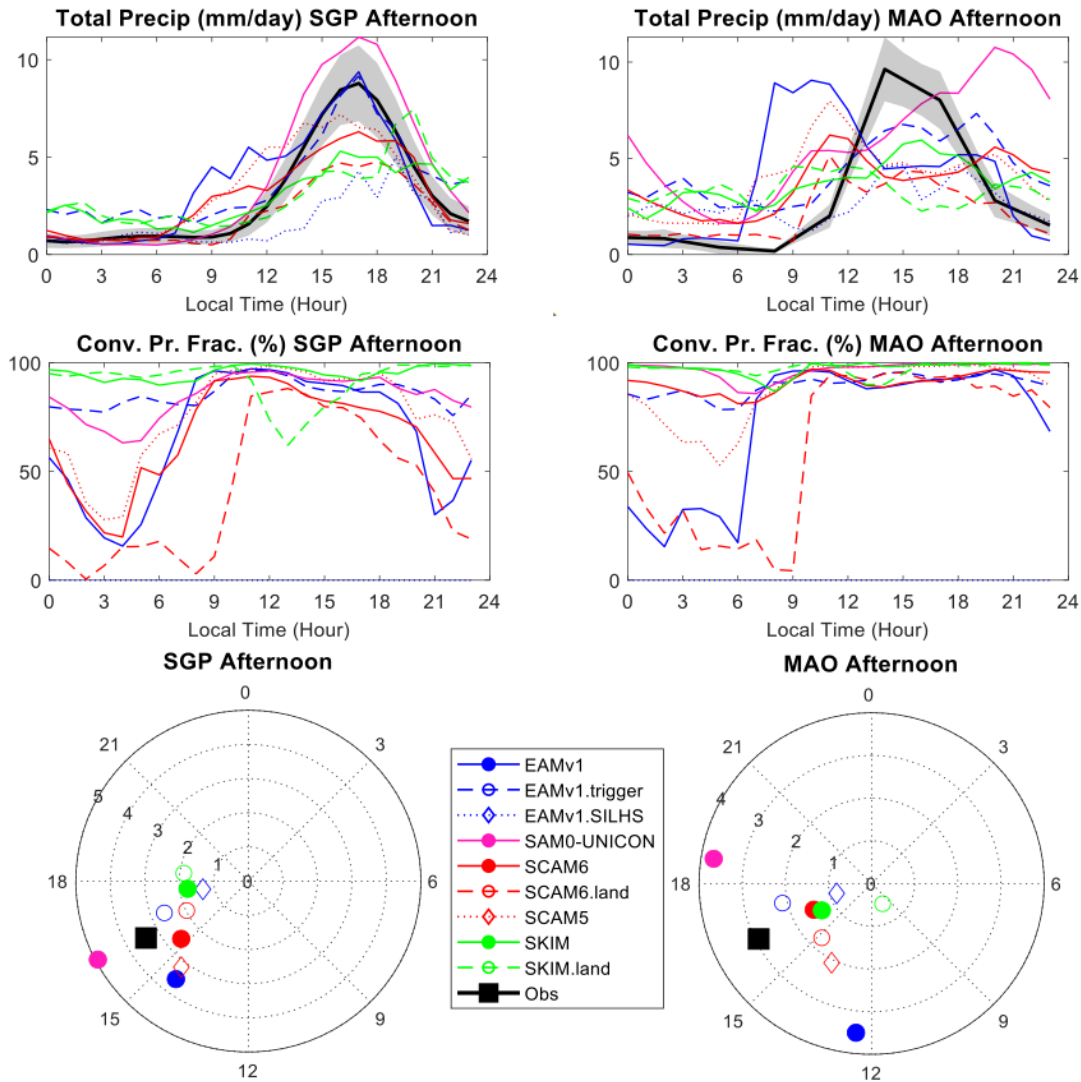


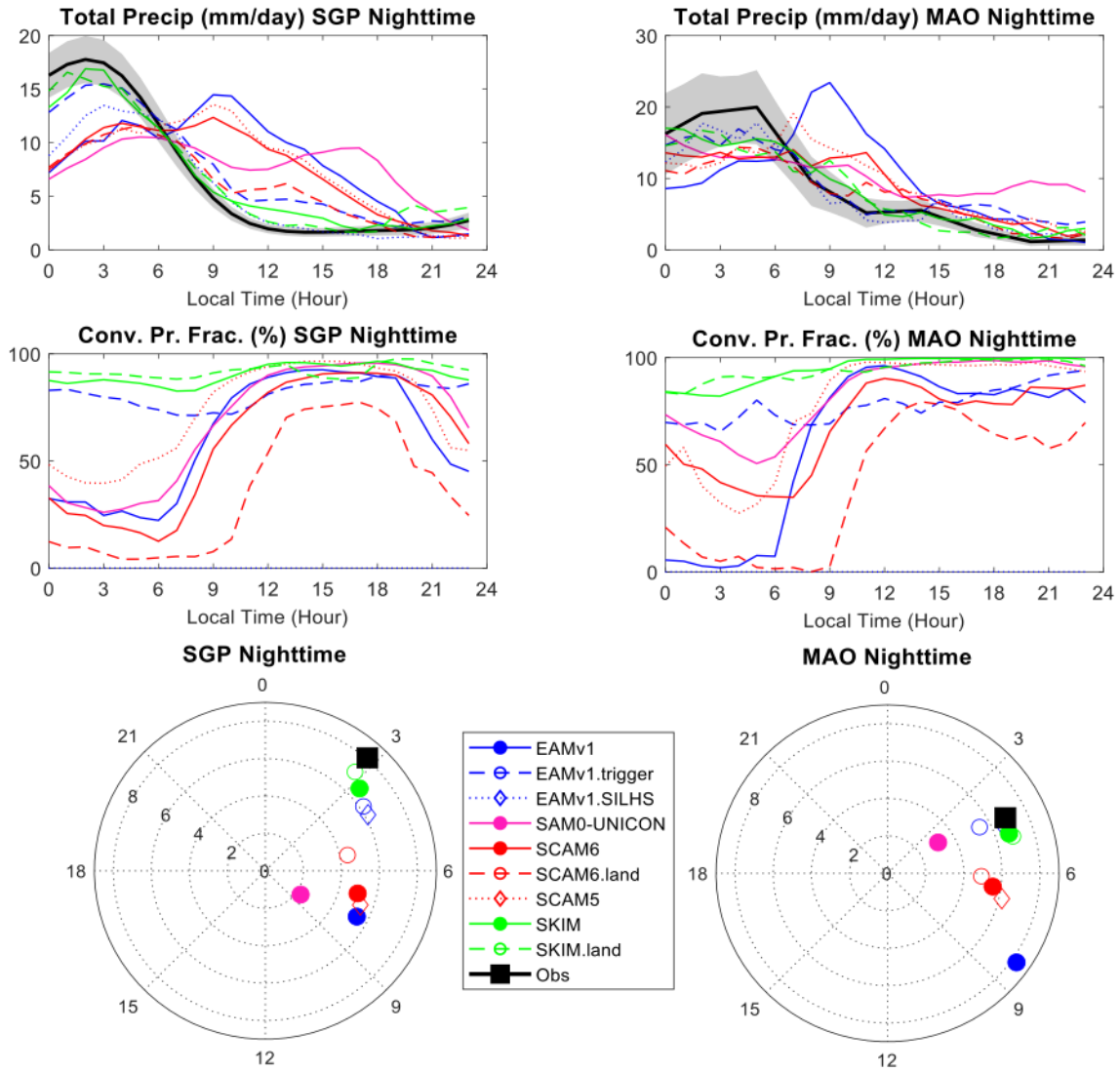
Figure 12: Q_1 and Q_2 averaged between 00 and 06 LST for selected nocturnal precipitation days at (left) SGP and (right) MAO.



1155

1156 Figure 13: As in Figure 6 but for selected models/configurations for sensitivity study. Sensitivity
 1157 runs are indicated by dashed/dotted lines and open symbols. Note that the convective
 1158 precipitation fraction for EAMv1.SILHS (blue dotted line) is zero because the convective and
 1159 large-scale precipitation is unified in CLUBB-SILHS.

1160



1161

1162 Figure 14: As in Figure 13 but for nocturnal precipitation days.

1163

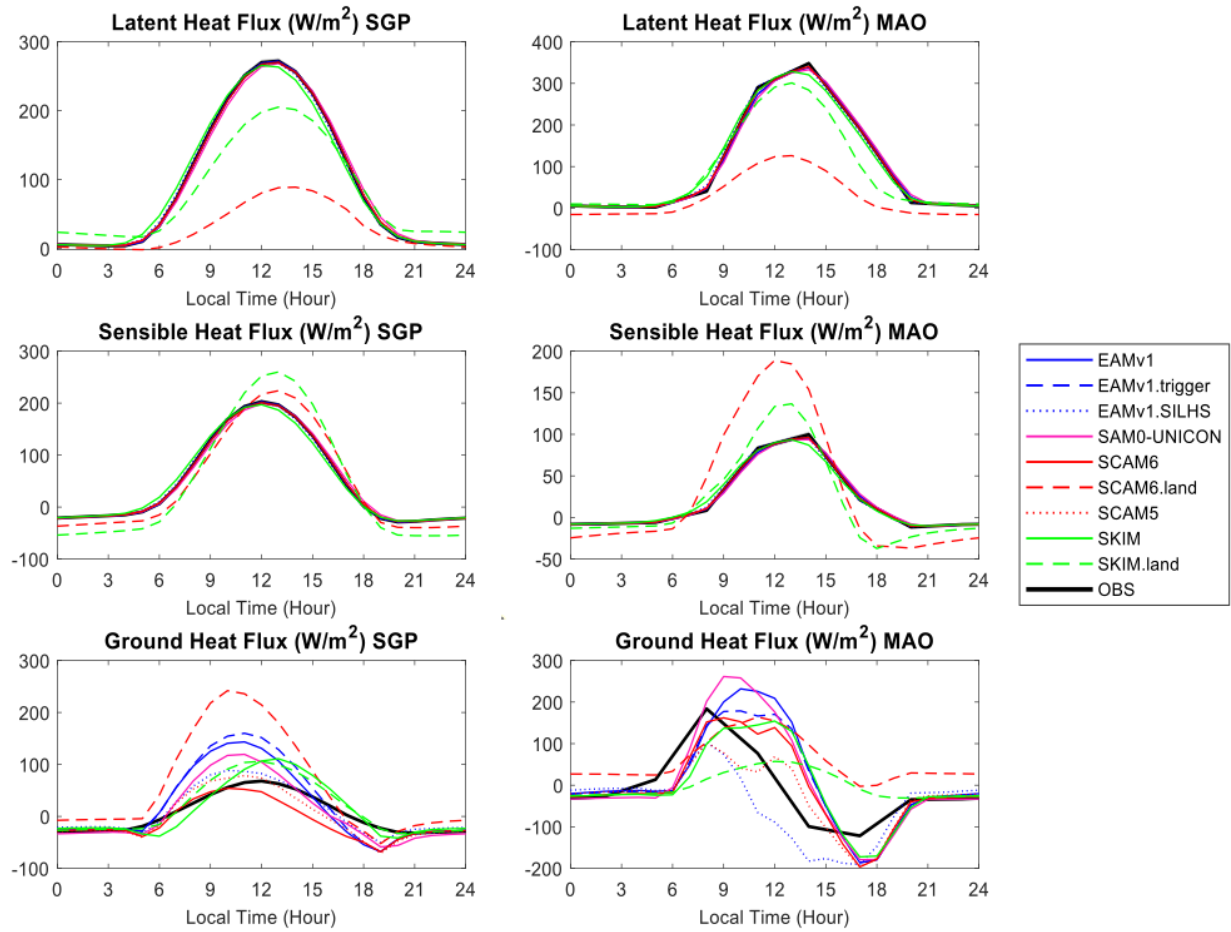


Figure 15: The diurnal cycle of (top) surface latent heat, (middle) sensible heat fluxes and (bottom) ground heat flux (net radiative fluxes minus latent and sensible heat fluxes) averaged for the long-term simulation periods at (left) SGP and (right) MAO. The diurnal cycle averaged in afternoon and nocturnal precipitation days have similar performance (not shown).